Study and control of polarization in a ground-based quantum communication telescope

Master thesis realized with the aim of obtaining the degree of Master in Aerospace Engineering

Martin Hubert

Promoters:

Vincent Moreau
Serge Habraken

Jury:

Vincent Moreau
Serge Habraken
Jérôme Loicq
Marc Georges

University of Liège
Faculty of Applied Sciences

Academic year 2023 - 2024

Acknowledgments

First of all, I would like to sincerely thank my industrial promoter, Vincent Moreau, whose clarity of mind and ability to explain concepts simply but qualitatively were major factors in the smooth running of this end-of-study project. I would also like to thank my academic promoter, Serge Habraken, for always encouraging and congratulating me on my work during our various interviews, and for his vision and professional knowledge of the subject, which enabled me to consider all aspects of the problems and difficulties encountered in order to gain a better understanding of them.

I also thank my parents, who have never doubted my abilities and have always admired my work, as well as encouraging me along the path to success.

A final, but not least, thank you is dedicated to my maternal grandfather, who admires the culmination of this work, and my studies, from heaven. I thank him for always expressing his admiration for my academic achievements, as well as for the congratulations he never failed to give me.

Verlaine, June 10, 2024

Martin Hubert

Study and control of polarization in a ground-based quantum communication telescope

Martin Hubert

Supervisors: Moreau V., Habraken S.
Master in Aerospace Engineering, University of Liège
Academic year 2023-2024

Abstract

The vulnerability of classical encryption protocols to the increasing power of quantum computers is driving research into new and secure methods of communication. One promising candidate to address this problematic is quantum key distribution, which takes advantage of the properties of quantum mechanics to ensure a secure exchange of the encryption key, thus guaranteeing secure communication between the entities.

Quantum key exchange algorithms exploit the properties of quantum objects, typically the polarization of photons, to set up the secure exchange. To this end, the polarization state of the photons must be maintained throughout the exchange. Reflections of the telescope mirrors at the receiver, however, modify the polarization state.

The present work recalls the concept of light polarization, and the different types with the associated mathematical description. A general introduction to quantum key distribution, and to the MOCA project, then follows to introduce the reader to the main parts of this work, which focuses on characterizing the changes in polarization caused by the telescope, and in particular by the third mirror where the high angle of incidence causes polarization aberrations. Based on the Jones formalism, it is shown that the phase shift between the orthogonal components of the polarization at the wavelengths relevant to this project is too large to satisfy the requirements in terms of polarization extinction ratio.

As a result of the unsatisfactory performance of the telescope, an in-depth study of the use of birefringent crystals to correct the excessive phase shift is carried out, showing the need to use three crystals of different birefringence to achieve the desired polarization extinction ratios at the three relevant wavelengths for MOCA. Results also show that if there is an order of priority for optimizing the wavelengths of the application, the use of one or two crystals proves to be worthwhile. Eventually, based on ellipsometric measurements, the phase shift and change in polarization orientation generated by a mirror of configuration comparable to the third mirror of the telescope are determined. A comparison of the results provided by models to real measurements confirms the implementation of the Jones formalism and highlights the need to characterize a mirror on the basis of experimental measurements.

Acronyms

- ACS : Antenna Control System
- Al_2O_3 : Aluminum Oxide
- AMOS : Advanced Mechanical and Optical Systems
- AO : Adaptive Optics
- AOI : Angle Of Incidence
- BOC : Back-end Optical Conditioner
- CHIME : Copernicus Hyperspectral Imaging Mission for the Environment
- Cr : Chromium
- CV-QKD : Continuous-Variable Quantum Key Distribution
- DOP : Degree Of Polarization
- DV-QKD : Discrete-Variable Quantum Key Distribution
- ESA : European Space Agency
- FoV : Field-of-View
- HfO_2 : Hafnium Oxide
- INT-UQKD : International Use-case QKD
- MgF_2 : Magnesium Fluoride
- MOCA : Medium size Optical Communication Antenna
- NiCr : Nichrome
- OPD : Optical Path Difference
- PA : Polarization Aberrations
- PAT : Pointing, Acquisition and Tracking
- PER : Polarization Extinction Ratio(s)
- QKD : Quantum Key Distribution
- RAE : Rotating Analyzer Ellipsometer

- RPE : Rotating Polarizer Ellipsometer
- RSA : Rivest-Shamir-Adleman
- SALTO : Smart Adaptive-optics and Laser guide-star for medium-size Telescopes and Optical communications
- SiO_2 : Silicon Dioxide
- SNR : Signal-to-Noise Ratio
- Ta : Tantalum
- Ta_2O_5 : Tantalum Oxide
- ZnO : Zinc Oxide

Contents

Chapter 1

Introduction

1.1 Motivation

In our everyday lives, communication plays a fundamental role in the exchange of information between several entities. There are many and varied means of communication, the use of which varies according to the situation. If the exchange is to be private, it must be ensured that no third party intercepts any information.

For encrypted data, whose content is supposed to remain private, possession of a key enabling decryption is necessary in order to access the content. When this key is exchanged for this purpose between two entities, any interception by a third party would compromise the security of the operation, and the consequences could prove disastrous depending on the importance of the encrypted information. Numerous encryption algorithms have therefore been developed to secure information, ranging from the most rudimentary and therefore less reliable, such as Cesar code, to the most sophisticated and widely used today, such as RSA encryption.

Recently, the development of quantum physics has opened a new door to secure key exchanges. This new exchange possibility, called *quantum key distribution* (QKD), consists of a secure method of key exchange that discerns the presence of an intruder (eavesdropping) between two entities, commonly known as Alice and Bob[1], based on the physical principle that the presence of an observer disturbs the quantum system. What's more, as the power of quantum computers undermines encryption algorithms based on the limited computing power of today's computers, new methods such as QKD need to be put in place to guarantee the security of exchanges for the foreseeable future.

New quantum key exchange protocols such as BB84 and B92, based on Heisenberg's uncertainty principle, have emerged. Specifically, these protocols utilize a property of light called *polarization*. This property can be present for transverse waves, such as light, and corresponds by definition to the directions of vibration of the electric field components. Through the protocols developed for QKD, secure quantum key exchanges can take place by advantageously making use of polarized photons and of the principles of quantum mechanics.

The key characteristic of the previously mentioned quantum protocols being polarization state, it is important to ensure that the latter is maintained throughout the communication channel to enable the reception of the correct information. In particular, the ground receiving antenna, which takes the

[1] Alice being the one sending the information to Bob.

form of a telescope in the case of optical communications, must maintain the initial polarization state. However, reflections on the various mirrors of a telescope induce phase delays between the orthogonal components of polarization if the incidence is not normal. It is therefore necessary to determine these delays, and then correct them to maintain polarization, and more generally, the communicated information.

This is where the importance of this work lies, which primarily focuses on studying polarization changes through the telescope, particularly induced by the third mirror, and analyzes different ways to tackle this problem, with the aim of achieving good performances in transmitting the communicated information.

1.2 Goals of the project

The first objective of this project is to study changes in the polarization state of light as it propagates through an optical communication antenna, which takes the form of a telescope. The aim is to understand how the polarization state is affected by the optical components inside the telescope, using the Jones formalism useful for describing the polarization state of fully polarized light, as optical components can, by reflection, modify the polarization state.

Secondly, the main objective of this project is to determine a method for correcting phase shifts between orthogonal components of polarization. This is of major importance in terms of the performance of optical communication systems in maintaining polarization states, enabling secure and reliable exchanges via quantum key distribution.

1.3 Structure of the report

The present work is structured as follows:

Part I contains the necessary theoretical background to understand polarization, starting from Maxwell's equations to highlight the wave behavior of light, which forms the basis of polarization. It then introduces the various types of polarizations, along with the necessary mathematical formalism, ultimately leading to the Jones formalism, which is the fundamental framework used to describe the polarization state of fully polarized light.

Part II introduces the principle of quantum key distribution, and explains the associated quantum theory. The well-known BB84 quantum key exchange protocol is explained and its security analyzed. Finally, the QKD antenna project within AMOS is described, explaining its various parts, with particular attention to the optical design.

Part III uses the Jones formalism introduced earlier to characterize the telescope by its Jones matrix, and to deduce the change in polarization for the different types of polarization at the object scene. In addition, performance, i.e. the telescope's ability to retransmit the information correctly, is determined as a function of wavelength and type of polarization. It is also at this stage that the induced phase shifts are rigorously determined for subsequent correction.

Part IV is devoted to solving the problem of polarization degradation, i.e. correcting the phase shift between the orthogonal components of polarization by means of compensation. The methodology employed is based on the principle of birefringence, using crystals to achieve the performance targets set at the wavelengths relevant to the project.

Part V aims to validate the correct implementation of the Jones formalism, and consequently the correct characterization of the telescope model, by comparison with experimental measurements made on an ellipsometer. The ellipsometric parameters, i.e. the phase shift between the orthogonal components of polarization and the polarization orientation, of a mirror of a similar configuration to that causing the phase shifts in the telescope, are determined. A comparison with the results of the numerical model is carried out for final validation.

1.4 AMOS company

As part of my end-of-study work, I did an internship within the AMOS (Advanced Mechanical and Optical Systems) company. Founded in 1983, AMOS has distinguished itself for over 40 years in the development of ultra-high opto-mechanical systems, which are mainly dedicated to the space industry and professional astronomy. The main achievements of the company are professional-grade telescopes, optical systems for space applications, testing apparatus for space instruments, and precision mechanical equipment (Advanced Mechanical and Optical Systems (AMOS), 2024).

Part I

Theoretical background

Chapter 2

Polarized light

2.1 Electromagnetic radiation

2.1.1 Maxwell's equations

Electromagnetic radiation consists of an electric and magnetic field traveling through space, at constant speed depending on the medium. The full description of electromagnetic radiation is derived from Maxwell's equations, which describe all classical electromagnetic phenomena. These are given here under their differential form:

$$\overrightarrow{\nabla} \cdot \overrightarrow{D} = \rho, \tag{2.1}$$

$$\overrightarrow{\nabla} \cdot \overrightarrow{B} = 0, \tag{2.2}$$

$$\overrightarrow{\nabla} \times \overrightarrow{E} = -\frac{\partial \overrightarrow{B}}{\partial t}, \tag{2.3}$$

$$\overrightarrow{\nabla} \times \overrightarrow{H} = \overrightarrow{J} + \frac{\partial \overrightarrow{D}}{\partial t}. \tag{2.4}$$

$\overrightarrow{E}$ stands for the electric field vector, $\overrightarrow{D}$ for the electric displacement vector, $\overrightarrow{B}$ for the magnetic induction vector and $\overrightarrow{H}$ for the magnetic field vector. The density of free charges is given by ρ, and the current density by $\overrightarrow{J}$. In a linear, homogeneous and isotropic material, the electric displacement and magnetic induction vectors are linked to the electric field and magnetic field vectors by constitutive equations of the form:

$$\overrightarrow{D} = \varepsilon \overrightarrow{E}, \tag{2.5}$$

$$\overrightarrow{B} = \mu \overrightarrow{H}, \tag{2.6}$$

with ε the permittivity, and μ the permeability, of the medium. Moreover, in a conducting medium, the current density is linked to the electric field by the electrical conductivity σ:

$$\overrightarrow{J} = \sigma \overrightarrow{E}. \tag{2.7}$$

2.1.2 Wave equation for electric and magnetic fields

Maxwell's equations can be used to obtain the wave equation for the electric field $\overrightarrow{E}$ and magnetic field $\overrightarrow{H}$. Vanderheyden (2023) proposes the following approach:

Taking the curl of Equation 2.3,

$$\overrightarrow{\nabla} \times \left(\overrightarrow{\nabla} \times \overrightarrow{E} \right) = \overrightarrow{\nabla} \times \left(-\frac{\partial \overrightarrow{B}}{\partial t} \right) = -\frac{\partial \left(\overrightarrow{\nabla} \times \overrightarrow{B} \right)}{\partial t}, \tag{2.8}$$

and using the vectorial calculus relation

$$\overrightarrow{\nabla} \times \left(\overrightarrow{\nabla} \times \overrightarrow{E} \right) = \overrightarrow{\nabla} \left(\overrightarrow{\nabla} \cdot \overrightarrow{E} \right) - \overrightarrow{\nabla}^2 \overrightarrow{E}, \tag{2.9}$$

one has

$$\overrightarrow{\nabla} \times \left(\overrightarrow{\nabla} \times \overrightarrow{E} \right) = \overrightarrow{\nabla} \frac{\rho}{\varepsilon} - \overrightarrow{\nabla}^2 \overrightarrow{E}, \tag{2.10}$$

$$= -\frac{\partial \left(\overrightarrow{\nabla} \times \overrightarrow{B} \right)}{\partial t}, \tag{2.11}$$

$$= -\mu\sigma \frac{\partial \overrightarrow{E}}{\partial t} - \mu\varepsilon \frac{\partial^2 \overrightarrow{E}}{\partial t^2}. \tag{2.12}$$

Eventually, the wave equation for the electric field is

$$\overrightarrow{\nabla}^2 \overrightarrow{E} - \mu\varepsilon \frac{\partial^2 \overrightarrow{E}}{\partial t^2} = \mu\sigma \frac{\partial \overrightarrow{E}}{\partial t} + \overrightarrow{\nabla} \frac{\rho}{\varepsilon}. \tag{2.13}$$

Similar manipulations can be applied to Equation 2.4 to obtain the wave equation for the magnetic field (see Appendix A):

$$\overrightarrow{\nabla}^2 \overrightarrow{H} - \mu\varepsilon \frac{\partial^2 \overrightarrow{H}}{\partial t^2} = \mu\sigma \frac{\partial \overrightarrow{H}}{\partial t}. \tag{2.14}$$

2.1.3 Propagation of uniform plane waves in vacuum

In free space, $\overrightarrow{J} = \overrightarrow{0}$ and $\rho = 0$, and Equations (2.13) and (2.14) reduce to

$$\overrightarrow{\nabla}^2 \overrightarrow{E} - \mu_0 \varepsilon_0 \frac{\partial^2 \overrightarrow{E}}{\partial t^2} = 0, \tag{2.15}$$

$$\overrightarrow{\nabla}^2 \overrightarrow{H} - \mu_0 \varepsilon_0 \frac{\partial^2 \overrightarrow{H}}{\partial t^2} = 0. \tag{2.16}$$

The solution is a plane wave propagating in the direction of the wave vector $\overrightarrow{k} = k_x \hat{x} + k_y \hat{y} + k_z \hat{z}$ with respect to the (x, y, z) coordinate system (Wolski, 2011):

$$\overrightarrow{E} = \overrightarrow{E_0} \cos\left(\overrightarrow{k} \cdot \overrightarrow{r} - \omega t + \phi_0 \right), \tag{2.17}$$

$$\overrightarrow{B} = \overrightarrow{B_0} \cos\left(\overrightarrow{k} \cdot \overrightarrow{r} - \omega t + \phi_0 \right), \tag{2.18}$$

with $\overrightarrow{E_0}$ and $\overrightarrow{B_0}$ the amplitudes of the electric and magnetic induction fields, respectively, ω the pulsation, and ϕ_0 a constant phase. The wave vector and the pulsation are linked to the frequency f and wavelength λ through

$$\omega = 2\pi f, \tag{2.19}$$

$$|\overrightarrow{k}| = \frac{2\pi}{\lambda}. \tag{2.20}$$

Moreover, the speed of the wave c_0 can directly be deduced from Equation 2.15 and Equation 2.16:

$$c_0 = \frac{1}{\sqrt{\mu_0 \varepsilon_0}} \approx 3 \cdot 10^8 \text{ m/s}. \tag{2.21}$$

As a consequence of Maxwell's equations, light is a transverse wave consisting of an electric and magnetic field perpendicular to each other, and oscillating in phase through space (Klein and Furtak, 1986).

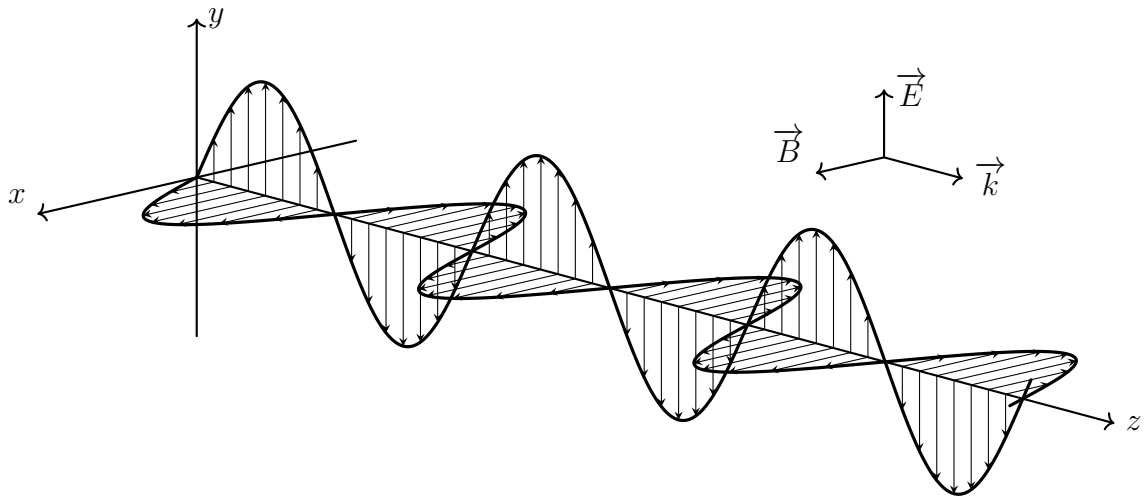

Figure 2.1 – Electromagnetic wave propagation in the case of an in-plane oscillation of $\overrightarrow{E}$ and $\overrightarrow{B}$, with $\overrightarrow{k} = \hat{z}$. *Adapted from Neutelings (2018).*

2.2 Wave polarization

The directions of the electric and magnetic fields within the plane perpendicular to the direction of propagation may change in function of position and time, depending e.g., in which medium the wave is propagating. The instantaneous orientations of the field vectors are in consequence necessary parameters in order to describe an electromagnetic wave.

Polarization is defined as *the electric field vector orientation as a function of time, at fixed position in space* (Hayt and Buck, 2001). As the electric field vector, electric displacement vector, magnetic field vector and magnetic induction vector are all linked through Maxwell's equations and through the constitutive relations, it is sufficient to specify the electric field direction only. However, the choice of the electric field over the magnetic field is motivated by the fact that the force experienced by electrons due to the electric field of light, when the latter interacts with matter, is greater than that experienced by electrons due to the magnetic field of light (Scharf, 2007).

The three types of polarization — linear, circular, and elliptical — are characterized by the ratio of the amplitudes of the electric field components and the phase shift between these. For the sake of illustration, fully polarized light is considered hereafter. The different types of polarization can be easily illustrated by considering an electromagnetic wave propagating through space in a direction $\overrightarrow{k} = \hat{z}$, with the electric field thus oscillating perpendicularly:

$$\overrightarrow{E}(z,t) = \overrightarrow{E_x}(z,t) + \overrightarrow{E_y}(z,t) = E_{0x} \cos(kz - \omega t + \varphi_x)\,\hat{x} + E_{0y} \cos(kz - \omega t + \varphi_y)\,\hat{y}. \tag{2.22}$$

2.2.1 Linear polarization

When the electric field vibrations are restricted to one single plane oriented along the direction of propagation, light is said to be linearly polarized. The necessary and sufficient condition to obtain linear polarization is to have a phase shift[1] $\delta = \varphi_y - \varphi_x$ equal to zero or any multiple of π, i.e.

$$\delta = k\pi, \qquad \text{with} \qquad k \in \mathbb{Z}, \tag{2.23}$$

as each field component will then always have a cosinusoidal behavior. The plane orientation α with respect to x-axis is characterized by the ratio of the amplitudes of each component:

$$\tan\alpha = \frac{E_{0y}}{E_{0x}}. \tag{2.24}$$

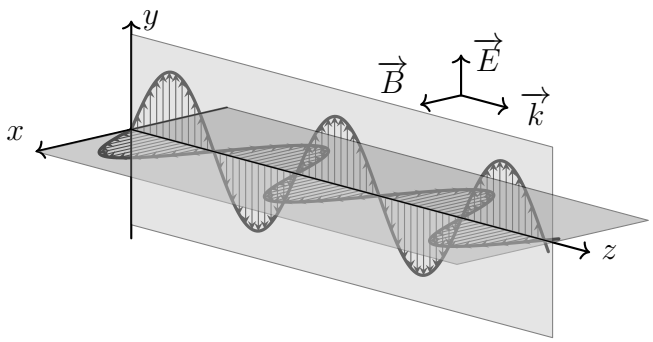

Figure 2.2 – **Vertical linear polarization**. The wave vector $\vec{k}$ lies along the z-axis. $x-z$ and $y-z$ planes represent the planes of oscillations of the magnetic and electric field, respectively. *Adapted from Neutelings (2018).*

The sign of the right-hand side defines if the plane orientation will be in the interval $[0°, 90°]$ or not, depending on the type of oscillations the electric field components present : *in-phase* or *out-of-phase* oscillations. For each type, the field component writes

$$\begin{cases} \vec{E}_y = E_{0y}\cos(kz-\omega t)\,\hat{y} & \text{if} \quad \delta = 2k\pi, \text{ with } k \in \mathbb{Z}, \\ \vec{E}_y = -E_{0y}\cos(kz-\omega t)\,\hat{y} & \text{if} \quad \delta = (2k+1)\pi, \text{ with } k \in \mathbb{Z}, \end{cases} \tag{2.25}$$

respectively. Both cases with equal absolute field amplitudes, i.e. $\alpha = 45°$ and $\alpha = -45°$, are called linear polarization at $45°$, and $-45°$, respectively. Other interesting cases are horizontal and vertical polarization, for which $E_{0y} = 0$ and $E_{0x} = 0$, respectively. These four special cases are useful for QKD as will be introduced in Chapter 3.

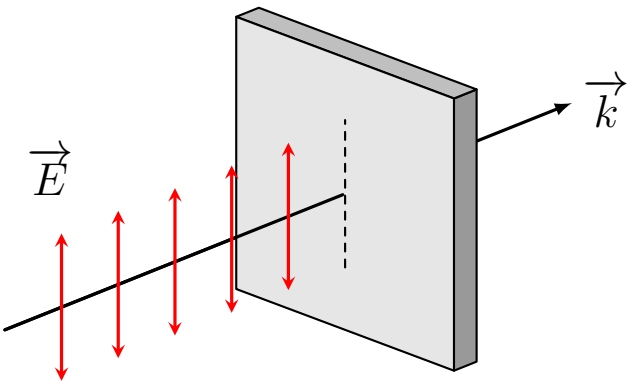

Figure 2.3 – **Vertical linear polarization**. *Adapted from Tsagkaropoulos (2021).*

[1] Choosing $\varphi_x = 0$ as a reference, one has $\delta = \varphi_y - \varphi_x = \varphi_y$.

2.2.2 Circular polarization

If one considers a fixed position along the z-axis, and allows time to vary, there exists a configuration in which the electric field vector draws a circle. Light is then said to be circularly polarized. Two conditions must be fulfilled in order to obtain circularly polarized light:

$$\delta = \pm\frac{\pi}{2} + 2k\pi \qquad \text{with} \qquad k \in \mathbb{Z}, \tag{2.26}$$

$$E_{0x} = E_{0y} = E_0. \tag{2.27}$$

The corresponding field components are:

$$\overrightarrow{E}_x = E_0 \cos(kz - \omega t)\,\hat{x}, \tag{2.28}$$

$$\overrightarrow{E}_y = \mp E_0 \sin(kz - \omega t)\,\hat{y}. \tag{2.29}$$

Indeed, the expression of a circle can be obtained from the amplitude:

$$|\overrightarrow{E}|^2 = |\overrightarrow{E}_x + \overrightarrow{E}_y|^2 = E_0^2 \cos^2(kz - \omega t) + E_0^2 \sin^2(kz - \omega t) = E_0^2, \tag{2.30}$$

and the constant amplitude, corresponding to the radius of the circle, is naturally equal to

$$|\overrightarrow{E}| = \sqrt{E_0^2 \cos^2(kz - \omega t) + E_0^2 \sin^2(kz - \omega t)} = E_0. \tag{2.31}$$

If $\delta = \pi/2 + 2k\pi$, the field vector rotates clockwise in the plane perpendicular to the direction of propagation, and the polarization is called *left-handed circular polarization*. When the field rotates counter-clockwise, i.e. $\delta = -\pi/2 + 2k\pi$, the polarization is called *right-handed circular polarization* (Hayt and Buck, 2001).

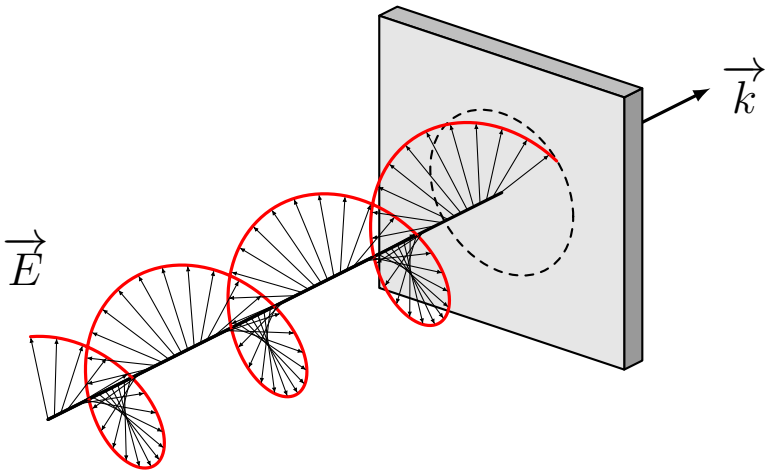

Figure 2.4 – **Right-handed circular polarization**. *Adapted from Tsagkaropoulos (2021).*

2.2.3 Elliptical polarization

This type of polarization is the most general polarization state, as the field components amplitudes and the phase shift are arbitrary. Linear polarization is in fact a particular case of elliptical polarization, with $\delta = k\pi$ ($k \in \mathbb{Z}$), and circular polarization also but with a fixed value for the three parameters $E_{0x} = E_{0y}$ and $\delta = \pm\pi/2 + 2k\pi$ ($k \in \mathbb{Z}$).

A full characterization of elliptical polarization relies on the *polarization ellipse*. Following Collett (2005)'s approach, the equation of an ellipse can be obtained from $\overrightarrow{E}_x$ and $\overrightarrow{E}_y$ (see Appendix A):

$$\frac{E_x(z,t)^2}{{E_{0x}}^2} + \frac{E_y(z,t)^2}{{E_{0y}}^2} - \frac{2E_x(z,t)E_y(z,t)}{E_{0x}E_{0y}}\cos\delta = \sin^2\delta. \tag{2.32}$$

This expression is valid for any case of polarization, and therefore also in particular for linear and circular polarization. For the former, Equation 2.32 simplifies to:

$$\frac{E_x(z,t)^2}{{E_{0x}}^2} + \frac{E_y(z,t)^2}{{E_{0y}}^2} = \pm\frac{2E_x(z,t)E_y(z,t)}{E_{0x}E_{0y}}, \tag{2.33}$$

for in-phase and out-of-phase oscillations, respectively. For circular polarization, it becomes:

$$E_x(z,t)^2 + E_y(z,t)^2 = E_0^2, \tag{2.34}$$

which is the equation of a circle of radius E_0. The orientation of the principal axis of the polarization ellipse with respect to the x-axis is given by the *azimuth angle* ψ:

$$\tan 2\psi = \frac{2E_{0x}E_{0y}}{E_{0x}^2 - E_{0y}^2}\cos\delta, \tag{2.35}$$

and the *ellipticity angle* χ writes

$$\sin 2\chi = \frac{2E_{0x}E_{0y}}{E_{0x}^2 + E_{0y}^2}\sin\delta. \tag{2.36}$$

Introducing the *auxiliary angle* α such that

$$\tan\alpha = \frac{E_{0y}}{E_{0x}}, \tag{2.37}$$

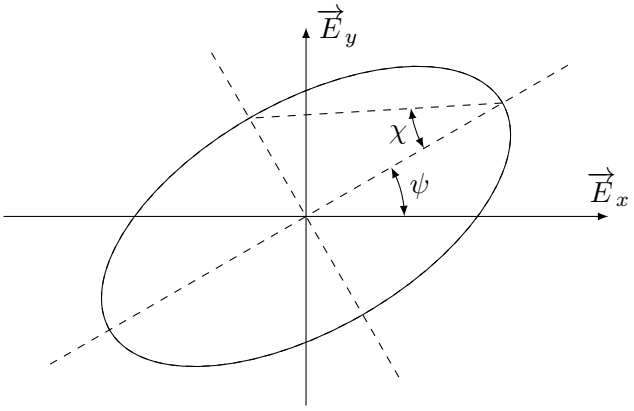

Figure 2.5 – **Polarization ellipse**. The azimuth angle characterizes the orientation of the principal axis of the ellipse, and the ellipticity angle provides information on the length of the secondary axis, therefore characterizing the phase shift between the components of the electric field.

the azimuth and ellipticity angles can be related through:

$$\tan 2\psi = \tan 2\alpha\cos\delta, \tag{2.38}$$

$$\sin 2\chi = \sin 2\alpha\sin\delta. \tag{2.39}$$

As for circular polarization, elliptical polarization is characterized by its handedness, making use of the same convention. Consequently, polarization can be *left-handed elliptical* or *right-handed elliptical*.

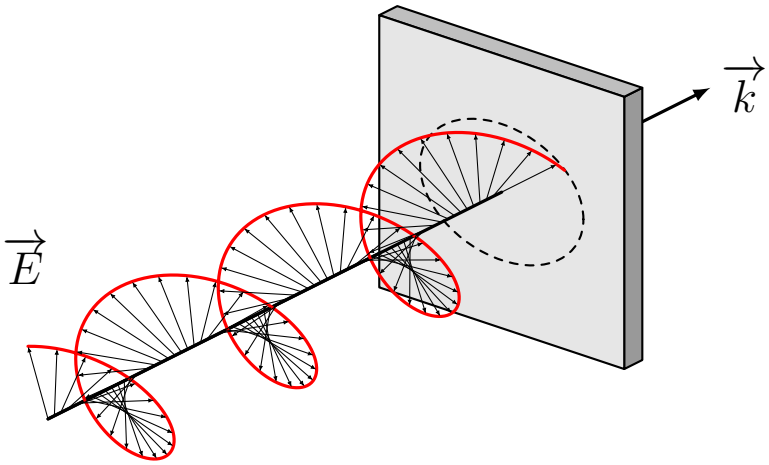

Figure 2.6 – **Right-handed elliptical polarization**. *Adapted from Tsagkaropoulos (2021).*

2.3 Description of the polarization state

2.3.1 Jones formalism

In the 1940s, R. Clark Jones published a series of papers introducing the Jones (matrix) formalism, which describes the state of polarization of completely polarized light (Scharf, 2007). It introduces the *Jones vector* to describe polarized light, and the *Jones matrix* to characterize optical elements with linear behavior. To fully describe the state of polarization and the propagation of plane waves, the amplitudes and phases of each field component must be fully stated (Jones, 1941). For the sake of illustration, light is considered as propagating along the z-axis, perpendicularly to the $x - y$ plane.

Jones vectors

The Jones vector comprises the transverse electric field components, hereafter written E_x and E_y:

$$\mathbf{E} = \begin{pmatrix} E_x \\ E_y \end{pmatrix} = \begin{pmatrix} E_{x0} e^{i\varphi_x} \\ E_{y0} e^{i\varphi_y} \end{pmatrix}. \tag{2.40}$$

$E_{x0}, E_{y0}, \varphi_x$ and φ_y are the respective amplitudes and phases of the components. The intensity I of the electric field is

$$I = \mathbf{E}\mathbf{E}^* = |E_x|^2 + |E_y|^2, \tag{2.41}$$

and in an equally equivalent manner, the Jones vector can be rewritten as

$$\mathbf{E} = \begin{pmatrix} E_{x0} \\ E_{y0} e^{i(\varphi_y - \varphi_x)} \end{pmatrix}, \tag{2.42}$$

with the same polarization and intensity, but with a phase shift φ_x compared to Equation 2.40. As the phase difference δ between the two components is a characterizing parameter for polarization characterization, and not the absolute phase of each component, one can consequently choose to shift the phase of one component and rewrite the other accordingly. $\delta_x = 0$ can be chosen for the sake of simplicity and illustration. Jones vectors are also often normalized to have a unitary intensity:

$$\mathbf{E} = \frac{1}{\sqrt{|E_x^2| + |E_y^2|}} \begin{pmatrix} E_x \\ E_y \end{pmatrix}. \tag{2.43}$$

Table 2.1 – **Jones vectors for examples of polarization states.**

Polarization state	**Normalized Jones vector**
Horizontal polarization (along the x-axis)	$\begin{pmatrix} 1 \\ 0 \end{pmatrix}$
Vertical polarization (along the y-axis)	$\begin{pmatrix} 0 \\ 1 \end{pmatrix}$
Linear polarization at $+45°$ w.r.t the x-axis	$\frac{1}{\sqrt{2}} \begin{pmatrix} 1 \\ 1 \end{pmatrix}$
Linear polarization at $-45°$ w.r.t the x-axis	$\frac{1}{\sqrt{2}} \begin{pmatrix} 1 \\ -1 \end{pmatrix}$
Left-handed circular polarization	$\frac{1}{\sqrt{2}} \begin{pmatrix} 1 \\ i \end{pmatrix}$
Right-handed circular polarization	$\frac{1}{\sqrt{2}} \begin{pmatrix} 1 \\ -i \end{pmatrix}$
Elliptical polarization (C_1, C_2 and δ are constants)	$\frac{1}{\sqrt{C_1^2+C_2^2}} \begin{pmatrix} C_1 \\ C_2 e^{i\delta} \end{pmatrix}$

Jones matrices

Jones matrices are 2×2 matrices describing the effect of polarization sensitive elements on the polarization state. The input polarization state $\mathbf{E}_{\text{in}}$ is transformed linearly to the output polarization state $\mathbf{E}_{\text{out}}$ by

$$\mathbf{E}_{\text{out}} = \mathbf{J} \times \mathbf{E}_{\text{in}} = \begin{pmatrix} J_{11} & J_{12} \\ J_{21} & J_{22} \end{pmatrix} \begin{pmatrix} E_x \\ E_y \end{pmatrix}. \tag{2.44}$$

The Jones matrix $\mathbf{J}$ describes the transformation of the Jones vector by reflection, retardation, rotation, absorption or transmission (Scharf, 2007), and its elements are complex if they affect the phase. The state of light propagating through an optical system composed of multiple optical elements modeled by Jones matrices is given by Equation 2.44, where $\mathbf{J}$ is the product of the individual Jones matrices of the optical elements. If these are written $\mathbf{J}_i$, with $i = 1, 2 \ldots N$ (N being the number of optical elements), the equivalent Jones matrix of the optical system is

$$\mathbf{J} = \mathbf{J}_N \times \mathbf{J}_{N-1} \times \ldots \times \mathbf{J}_2 \times \mathbf{J}_1, \tag{2.45}$$

and the output Jones vector

$$\mathbf{E}_{\text{out}} = \mathbf{J} \times \mathbf{E}_{\text{in}} = \mathbf{J}_N \times \mathbf{J}_{N-1} \times \ldots \times \mathbf{J}_2 \times \mathbf{J}_1 \times \mathbf{E}_{\text{in}} = \begin{pmatrix} J_{11} & J_{12} \\ J_{21} & J_{22} \end{pmatrix} \begin{pmatrix} E_x \\ E_y \end{pmatrix}. \tag{2.46}$$

Table 2.2 – **Examples of Jones matrices.**

Optical element	**Jones matrix**
Horizontal polarizer (x-axis)	$\begin{pmatrix} 1 & 0 \\ 0 & 0 \end{pmatrix}$
Vertical polarizer (y-axis)	$\begin{pmatrix} 0 & 0 \\ 0 & 1 \end{pmatrix}$
$\pm 45°$ polarizer w.r.t the x-axis	$\frac{1}{2}\begin{pmatrix} 1 & \pm 1 \\ \pm 1 & 1 \end{pmatrix}$
Left-handed circular polarizer	$\frac{1}{2}\begin{pmatrix} 1 & -i \\ i & 1 \end{pmatrix}$
Right-handed circular polarizer	$\frac{1}{2}\begin{pmatrix} 1 & i \\ -i & 1 \end{pmatrix}$

2.4 Unpolarized light

Section 2.2 provides a general introduction to wave polarization for the various possible cases, together with the corresponding mathematical formalism. Transverse waves such as electromagnetic radiation are, however, not necessarily (fully) polarized, and in this case, the oscillations of the electric field no longer occur in certain preferential directions. The *degree of polarization* (DOP) is a measure of the portion of polarized light. It is defined as the ratio of the intensity of the polarized portion of light to the total intensity. The DOP is equal to 100% for fully polarized light, and to 0% for completely unpolarized light. This parameter is, as expected, independent of the choice of reference for the description of this type of light.

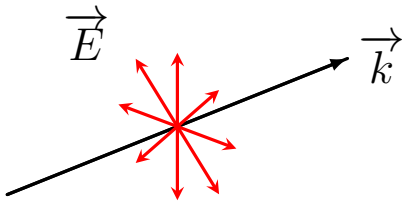

Figure 2.7 – **Unpolarized light**.

QKD requires fully polarized light. A description of the opposite case is therefore not necessary for the sake of this project. However, as the literature on the subject is vast, the reader can for instance refer to the work of Born and Wolf (1999) for a description of the Stokes formalism, and to the work of Scharf (2007) on Mueller matrices, for an analogy to the Jones formalism and matrices for unpolarized or partially polarized light.

Part II

Quantum Key Distribution

Chapter 3

Quantum Key Distribution

3.1 Principle of QKD

The ability to communicate securely without fear of interception or eavesdropping by others is paramount for sensitive applications, such as sharing an encryption key. The vulnerability of actual protocols to the increasing computing power of computers, as well as the quantum computer, are good reasons to turn to *quantum cryptography*, and more particularly, the distribution of quantum key, which takes advantage of quantum mechanics to enable secure exchange of information. In particular, QKD relies on the superposition principle and the no-cloning theorem to guarantee the security of the exchange (Wolf, 2021). For now, QKD has been achieved through optical fiber, and in free space, with success over distances of the order of several tens or even hundreds of kilometers. However, attenuation throughout the channel as well as the signal-to-noise ratio (SNR) limit the possible distance of exchange. Satellites are, however, good candidates to allow QKD over even longer distances (Wang et al., 2013).

The emergence of quantum mechanics has thus opened the doors to a new world of safe communications, for which quantum key exchange algorithms have been developed, such as BB84 and B92. In fact, all current discrete-variable[1] quantum key exchange protocols are variants of the BB84 protocol, which should therefore be explained in more detail. The following discussion on the latter is based on the work of Wolf (2021).

3.1.1 Qubits

Understanding quantum key exchange protocols requires understanding quantum bits, commonly called *qubits*. A qubit is a two-state quantum mechanical system, which is the quantum mechanical analog of a classical bit. Qubits have the particularity, unlike classical bits, to be in the superposition of two orthogonal states $|0\rangle$ and $|1\rangle$. These are for instance denoted $|H\rangle$ and $|V\rangle$ in the rectilinear basis[2], and $|D\rangle$ and $|A\rangle$ in the diagonal basis, corresponding respectively to the horizontal and vertical states, and to the diagonal and antidiagonal states. Qubits can be described by a linear combination of these states, i.e.

$$|\psi\rangle = \alpha|0\rangle + \beta|1\rangle, \tag{3.1}$$

[1] In opposition to continuous-variable quantum key distribution (CV-QKD), in which a continuous beam of light is sent through the channel instead of polarized photons one at a time as in discrete-variable quantum key distribution (DV-QKD) (Zhang et al., 2024).

[2] Orthogonal state pairs are referred to as a basis.

with $\alpha, \beta \in \mathbb{C}$, representing the probability amplitudes (Dawar, 2007). When measuring the qubit ψ, the probability of the outcome $|0\rangle$ is $|\alpha|^2$, and $|\beta|^2$ for the $|1\rangle$ outcome. As $|\alpha|^2$ and $|\beta|^2$ are probabilities, it follows that

$$|\alpha|^2 + |\beta|^2 = 1. \tag{3.2}$$

Four states are useful for the protocol described hereafter, namely horizontal, vertical, diagonal and antidiagonal.

Table 3.1 – **Dirac notation of qubits states.**

State	**Rectilinear basis**	**Diagonal basis**
Horizontal ($\|H\rangle$)	$\|0\rangle$	$\frac{1}{\sqrt{2}}(\|0\rangle - \|1\rangle)$ or $\frac{1}{\sqrt{2}}(-\|0\rangle + \|1\rangle)$
Vertical ($\|V\rangle$)	$\|1\rangle$	$\frac{1}{\sqrt{2}}(\|0\rangle + \|1\rangle)$ or $\frac{1}{\sqrt{2}}(-\|0\rangle - \|1\rangle)$
Diagonal ($\|D\rangle$)	$\frac{1}{\sqrt{2}}(\|0\rangle + \|1\rangle)$ or $\frac{1}{\sqrt{2}}(-\|0\rangle - \|1\rangle)$	$\|0\rangle$
Antidiagonal ($\|A\rangle$)	$\frac{1}{\sqrt{2}}(\|0\rangle - \|1\rangle)$ or $\frac{1}{\sqrt{2}}(-\|0\rangle + \|1\rangle)$	$\|1\rangle$

Qubits are realized using polarized photons for the sake of projects such as this one where photons are used as carriers of information. Other possibilities, such as the spin of electrons, exist to represent qubits. Polarization splitters allow deflecting polarized photons differently according to their state. For instance, a rectilinear splitter will deflect vertically and horizontally polarized photons differently, each reaching a different detector. A randomly linearly polarized photon will, however, be randomly deflected in one direction with probability $|\alpha|^2$ and in the other one with $|\beta|^2$ probability, as this state is the superposition of a horizontal and vertical state (see Equation 3.2).

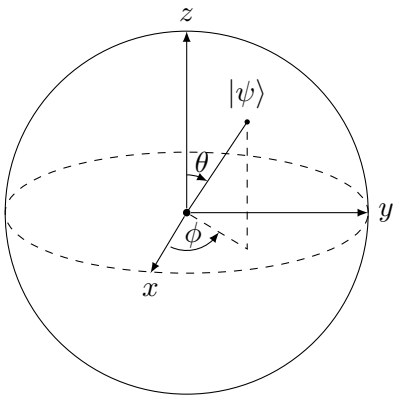

Figure 3.1 – **Bloch sphere representation of a qubit.** $\alpha = \cos\frac{\theta}{2}$, and $\beta = e^{i\phi}\sin\frac{\theta}{2}$, are the Hopf coordinates (Glendinning, 2005). Classical bits can only be located at the poles. *Adapted from Riebesell and Bringuier (2020).*

As a result, there is an equal probability of observing a diagonally polarized photon being deflected as a horizontally polarized photon or as a vertically polarized photon: 50% for each case. Here appears a very useful property of quantum mechanics that, as will be explained hereafter, allows secure communications : *measurement fixes the state.* A randomly polarized photon will, after passing through a polarization splitter, always be in one of the two possible states of the basis.

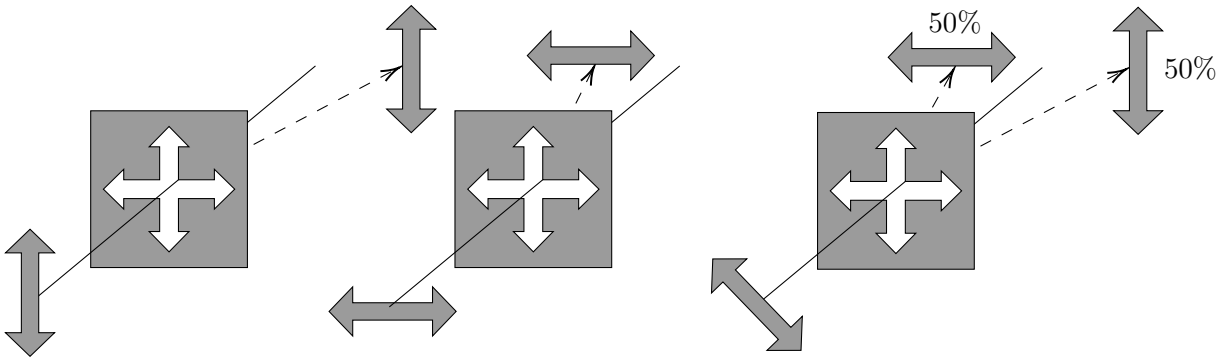

Figure 3.2 – **Polarization splitters**. A horizontally polarized photon is deflected to the left, while a vertically polarized photon is deflected to the right. In the case of a photon polarized in the diagonal basis, deflection will be to the left in 50% of the time, and to the right in 50% of the time too. *Adapted from Wolf (2021).*

3.1.2 BB84 protocol

BB84, developed in 1984 by Charles Bennett and Gilles Brassard, is the first QKD protocol, and relies on qubits. Two authorized parties, *Alice* and *Bob*, want to share a secret key over a certain distance. To achieve this, they use two channels. The initial channel is a classical channel, through which Alice and Bob can exchange messages in a classical way. Authentication is required for this channel, which means that Alice and Bob must identify themselves beforehand. *Eve*, a malicious person who wants to eavesdrop and gain information, can intercept the transmitted messages but cannot modify them. The second channel is a quantum channel, allowing Alice and Bob to transmit quantum signals (polarized photons). This channel is totally insecure, allowing Eve to manipulate the information. The BB84 protocol is composed of two steps: the *quantum transmission* step and *classical post-processing* step.

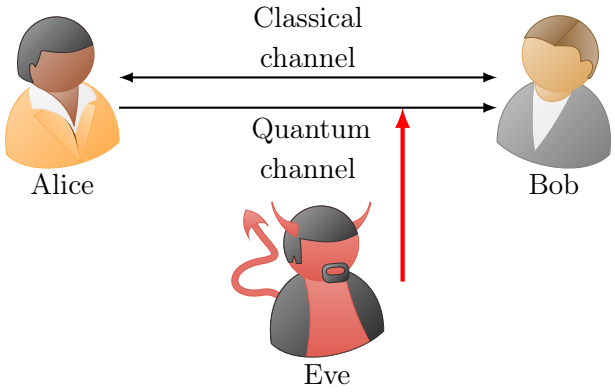

Figure 3.3 – **Fundamental configuration of the BB84 protocol**.

Quantum transmission

The quantum transmission phase encompasses all actions performed on quantum states, such as encoding and decoding classical bits into quantum states, as well as communication over the quantum channel. The process is as follows:

1. Alice chooses a string of classical bits, s.
2. For each bit, Alice randomly chooses a basis b (*rectilinear* $+$ or *diagonal* $\times$).
3. Alice encodes the string of bits s with photons polarized according to the basis. In the rectilinear basis, horizontal polarization corresponds to 0 and vertical polarization to 1. In the diagonal basis, diagonal polarization corresponds to 0 and antidiagonal polarization to 1 (see Table 3.1).

4. Bob chooses for each photon that he receives a basis to measure it, in order to obtain classical bits. Both Alice and Bob now have a classical bit string.

Table 3.2 – **Quantum transmission.**

String of chosen bits (s)	0	1	1	1	0	0	1
Random sending basis (b)	⤫	⤫	+	⤫	+	+	+
Photon sent by Alice	↗	↘	↕	↘	↔	↔	↕
Random receiving basis ($\tilde{b}$)	⤫	+	+	⤫	⤫	+	⤫
Photon measured by Bob	↗	↔	↕	↘	↗	↔	↗
String of received bits ($\tilde{s}$)	0	0	1	1	0	0	0

Classical Post-Processing

The remaining part of the protocol is classical. Alice and Bob exchange a series of classical information to derive from the bit strings they possess a shared secret key.

5. *Sifting step* : Bob publicly announces the bases he used to measure Alice's photons. Alice then compares Bob's bases with her own and tells for which photons the bases were the same. All bits for which the bases are different are discarded.

6. *Parameter estimation step* : In order to compute the *error rate*, which is the number of corresponding bits that differ, Bob reveals some bits of his key. If there is no eavesdropping, these bits are the same, and Alice confirms. However, if the error rate is too high, the protocol is stopped as there is eavesdropping[3]. Bits revealed in this step are discarded as they are now public.

7. *Error correction* and *privacy amplification steps* : By making use of error correction protocols, Alice and Bob erase the errors in their bit strings. These steps also try to reduce Eve's knowledge of the key, but weren't present in the initial proposal of the BB84 protocol. The reader can refer to the work of Wolf (2021) for detailed explanations on these steps.

[3]Even in the absence of an eavesdropper, errors might arise from noise in the channel. This is the reason why there is a certain threshold for the error rate.

Table 3.3 – **Classical Post-Processing.**

Sending basis (b)	⤫	⤫	✢	⤫	✢	✢	✢
Receiving basis ($\tilde{b}$)	⤫	✢	✢	⤫	⤫	✢	⤫
Matching bases ($b = \tilde{b}$)	✓	✗	✓	✓	✗	✓	✗
Sifting step (no eavesdropping)	0	–	1	1	–	0	–
Parameter estimation step	–	–	1	–	–	0	–
Confirmation of Alice	–	–	✓	–	–	✓	–

Security of the protocol

The security of the protocol is ensured by the principle of quantum mechanics that states that measuring a system disturbs its state. Eve's presence can potentially be highlighted thanks to this property. Consider for instance the first bit sent by Alice to Bob, as in table Table 3.2, but with the presence of an eavesdropper:

Table 3.4 – **Example of eavesdropping.**

Bit sent	0
Sending basis	⤫
Photon sent by Alice	↗
Eve's basis	✢
Eve's measurement	↔
Receiving basis	⤫
Photon measured by Bob	↘
Received bit	1

As Eve chose a different basis than Alice, the outcome of the measurement is random, with equal probability (50%) to obtain a horizontally or vertically polarized photon. In this particular case, a horizontally polarized photon was obtained. As Bob's basis is different from Eve's basis, when he measures this photon, the outcome is random and the probability of having a diagonal or antidiagonal state is the same (50%). In this case, an antidiagonal state is obtained, and the presence of Eve can be highlighted. Figure 3.4 illustrates all the possibilities for the outcome state of a photon sent by Alice to Bob, in the case of eavesdropping:

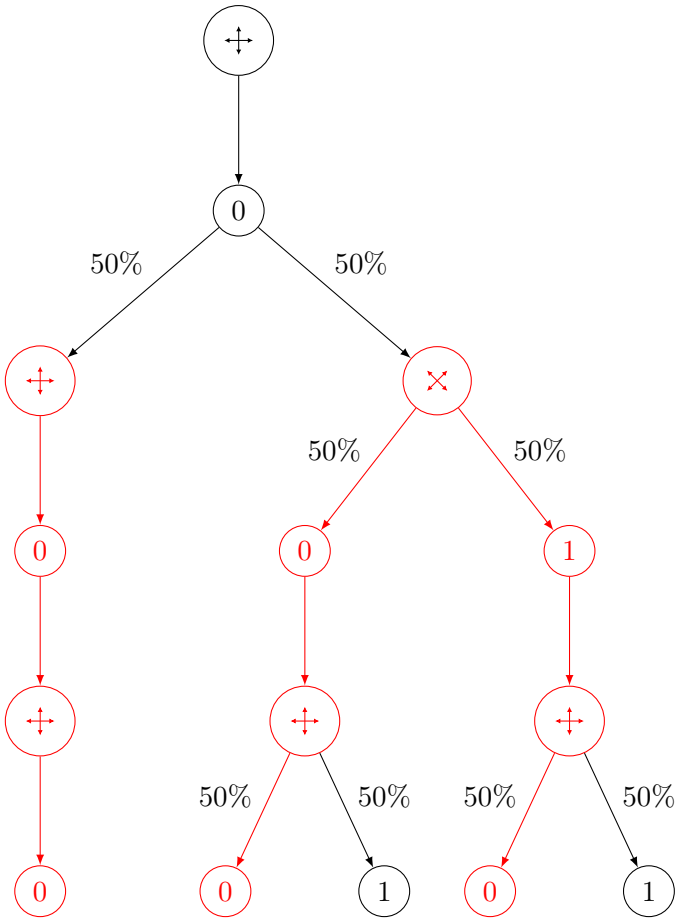

Figure 3.4 – **Possible outcomes for a bit sent by Alice to Bob with eavesdropping in the case of same bases for Alice and Bob**. Example with the rectilinear basis (extension to the diagonal basis yields the same results). The type of bit sent (0 or 1) does not matter. Eve's possibilities of not being detected are shown in red. *Adapted from Chaabani (2023).*

Two outcomes can highlight Eve's presence, as in two cases the bit measured by Bob, in the same basis as the one used by Alice, is different from the bit sent by Alice. Both cases are equiprobable, with 12.5% chance of happening.

The probability to have a flip of the bit is thus 25%, meaning that the probability of Eve not being detected is larger than the probability to be detected. However, for an increasing number of bits sent n, the probability to be detected evolves as

$$P_{D_E}(n) = 1 - \left(\frac{3}{4}\right)^n, \tag{3.3}$$

with $P_{D_E}(n)$ the probability to detect Eve using n bits. The probability increases rapidly, and in function of a chosen threshold value, the exchange will be considered secure or not.

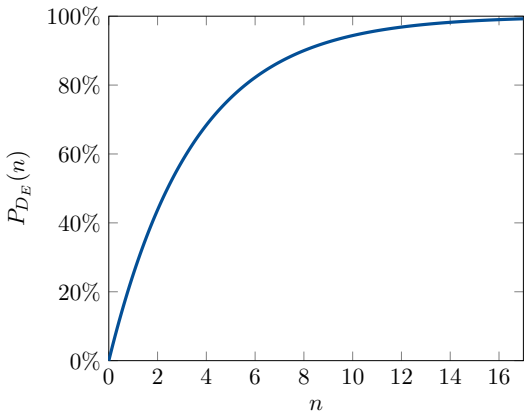

Figure 3.5 – **Probability to detect Eve in function of the number of bits used in the parameter estimation step.**

3.2 MOCA

3.2.1 Project overview

The MOCA (*Medium size Optical Communication Antenna*) project consists in the production of a cost-effective, medium-sized optical telecommunication antenna to be installed in Redu (Belgium). It is part of the INT-UQKD project (International Use Cases for operational QKD applications and services) of ESA (European Space Agency). The project, managed by RHEA System Luxembourg, has as main objective to develop and demonstrate international use cases for QKD, exploiting the BB84 and B92 protocols. The space segment part consists in the development of the *SpeQtral-1* satellite, by the SpeQtral company (Singapore), which will be launched in 2024/2025. A second satellite, *SpeQtre*, will be launched afterward. The quantum receiver box (QKD box) to be installed at the output of the antenna will be provided by the SpeQtral company. The antenna is made of:

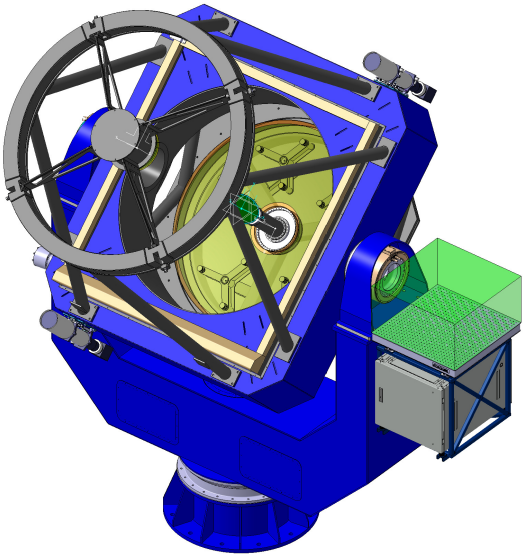

Figure 3.6 – **MOCA.**

- An optical tube, composed of several mirrors, which collects photons and bring them to the focal plane.
- A motorized altitude-azimuth mount designed to support the tube, ensuring precise alignment with the desired target area, while enabling tracking of an object in the sky.
- A back-end optical conditioner (BOC). It shapes the optical signal and splits it between the different instruments. This part includes the adaptive optics (AO), which compensate for atmospheric distortion. It also includes the polarization controller.
- A beacon emitter (auxiliary telescope), aligned with the optical tube, capable of sending a collimated laser beam to indicate antenna position.
- An antenna control system (ACS), to control and operate the antenna. It incorporates a pointing, acquisition and tracking (PAT) system, which guides the antenna to point toward the satellite, captures its beacon signal, and maintains tracking throughout the duration of the link.

The BOC and the auxiliary telescopes will be tested in factory and on the existing SALTO (Smart Adaptive-optics and Laser guide-star for medium-size Telescopes and Optical communications) telescope in Redu.

The project began in August 2023, and will be completed by September 2026. It is now entering the final step of the definition phase, which involves establishing the requirements, trade-offs and conceptual design, as well as defining the BOC. During the technology phase (that the project will enter soon), the design will be carried out in detail, the functioning of the various parts will be verified, and QKD will be validated by equipping SALTO with the MOCA BOC.

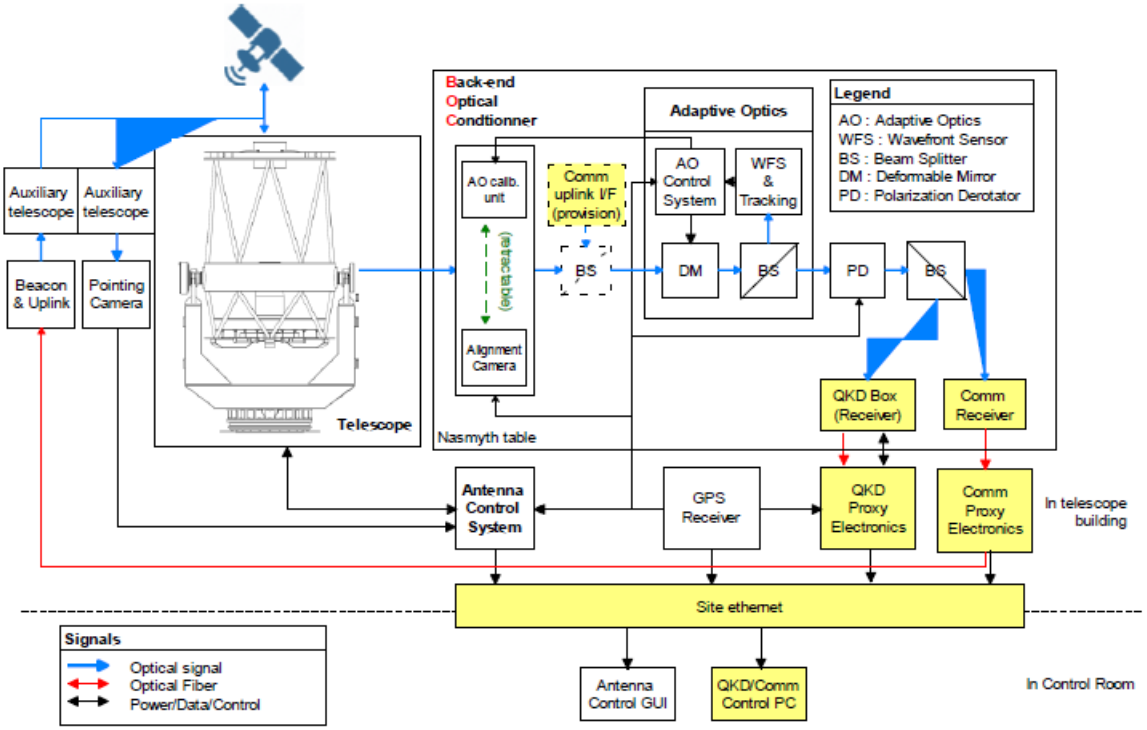

Figure 3.7 – **Functional block diagram of MOCA.** The yellow boxes indicate the components provided by RHEA System Luxembourg. Other subsystems are developed by AMOS.

3.2.2 Telescope optical design

The telescope design is a Nasmyth-type design[4] with a spherical concave primary mirror, elliptical convex secondary mirror and a folding third mirror. The design achieved integrates the benefits of a cost-effective spherical primary mirror, effective achromatic correction, and an easily accessible Nasmyth focus.

Table 3.5 – **Telescope design parameters.**

Configuration	Nasmyth
Aperture (entrance pupil)	1.5 m
Focal length	14.875 m
F-number	F/9.58
Field of view (FoV)	1.2 arcmin (± 0.01 degree)
Primary mirror	Concave spherical
Secondary mirror	Convex aspherical
Central obscuration	0.4 m (7.1% in surface)
Collimated beam diameter	21 mm

[4]The Nasmyth design is a modified version of the Cassegrain telescope design, with light reflected sideways.

The primary mirror M_1, defined as the entrance pupil, collects and converges the light toward the secondary mirror M_2. Thanks to the aspherical shape of the second mirror M_2, almost all spherical aberrations created by M_1 are corrected. Light is then reflected by the third mirror M_3, which retards the components of polarization by its orientation, toward the focal plane (FP). The latter still presents significant coma aberrations. All other aberrations are negligible, or compensated over the small size of the FoV. Moreover, the coatings of the three mirrors are made of protected silver.

Following the FP is the *corrector*. It is composed of the off-axis corrector and the pupil deformed mirror. The first component corrects for the remaining coma aberrations while the second has two functions: correcting for atmospheric distortion and for the spherical aberrations introduced by the off-axis corrector.

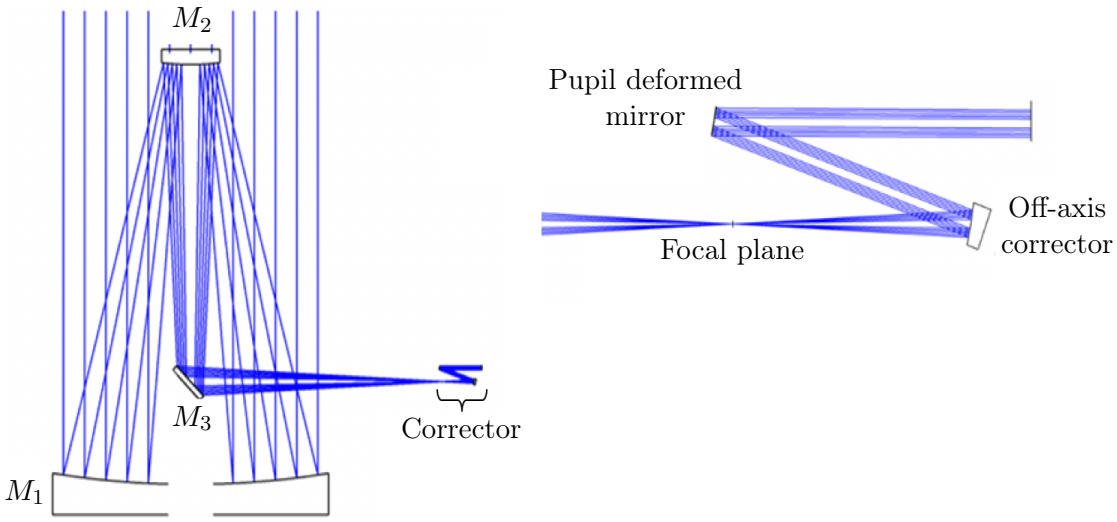

Figure 3.8 – **Telescope optical design.**

3.2.3 Optical communication wavelengths

Within the scope of this report, there are three main wavelengths to consider: QKD, *beacon* and *telecommunication*. The QKD wavelength, at 780 nm, is the one used in the main mission to implement quantum key exchange. Linearly polarized photons at this wavelength, which are required for quantum key exchange protocols, are therefore used.

Given the constant change in orientation of a satellite in space due to its own rotation, the polarization reference frame of the satellite also varies constantly. It is thus appropriate to use a beacon beam sending linearly polarized photons to MOCA to deduce the relative orientation of the satellite's polarization reference frame with respect to the reference frame of the terrestrial antenna. The measurement of the beacon polarization orientation is used to physically rotate the polarization of the QKD photons. The beacon photons have wavelengths of 685 nm for SpeQtral-1 and 1550 nm for SpeQtre. Finally, for SpeQtral-1, telecommunication is also possible using light at a wavelength of 1550 nm.

These cases are summarized in Table 3.6.

Table 3.6 – **Optical communication wavelengths.**

Satellite	**QKD**	**Beacon**	**Telecommunication**
SpeQtral-1	780 nm	685 nm	1550 nm
SpeQtre	780 nm	1550 nm	N/A

The wavelengths are imposed by SpeQtral, and correspond to the wavelengths used by the SpeQtral-1 and SpeQtre satellites as part of their mission. All wavelengths are therefore downlinked.

Part III

Telescope numerical model

Chapter 4

Telescope characterization

Chapter 2 describes electromagnetic radiation and polarization, and introduces the Jones formalism to characterize the polarization state of light. Moreover, the Jones formalism can also be used to model optical elements, such as waveplates, to deduce the outgoing polarization state from the incoming one. This, however, requires the knowledge of the Jones matrix of each optical element present in the optical system, i.e. in the telescope. A natural matrix multiplication along the optical path, as it is unique, can yield the equivalent Jones matrix of the telescope. Nevertheless, the individual Jones matrix of the different optical elements are not known a priori, and it is therefore necessary to think differently in order to determine the Jones matrix of the telescope. For this purpose, one can rely on knowledge of the polarization state of the light at the object scene and image of the telescope, and more precisely, on the knowledge of the components of the electric field and their phase shift, to proceed in reverse in order to derive the Jones matrix.

4.1 Jones matrix derivation

The telescope model made in the *Ansys Zemax OpticStudio* software allows analyzing the polarization state of light at each location of the optical path. Crucial information such as the electric field vector components and the phase delay between them can be determined. The problem is thus not to determine the polarization state at the telescope's image given the polarization state at the object scene, but to determine the Jones matrix of the telescope given the polarization state at the object scene and image:

$$\mathbf{E}_\mathrm{i} = \mathbf{J} \times \mathbf{E}_\mathrm{o}, \tag{4.1}$$

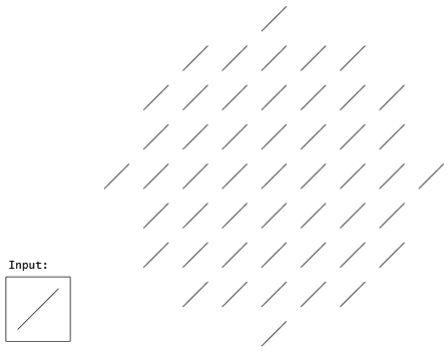

Figure 4.1 – **Polarization pupil map at the object scene**. Example with linear polarization at $+45°$ and $\lambda = 780$ nm. The spatial sampling is 9×9. Electric field components and their phase shift are obtained from here.

or written explicitly,

$$\begin{pmatrix} E_{x,i} \\ E_{y,i} \end{pmatrix} = \begin{pmatrix} J_{xx} & J_{xy} \\ J_{yx} & J_{yy} \end{pmatrix} \begin{pmatrix} E_{x,o} \\ E_{y,o} \end{pmatrix}, \tag{4.2}$$

with $\mathbf{J}$ being the Jones matrix, and its components are the unknowns. $E_{x,i}, E_{y,i}, E_{x,o}$ and $E_{y,o}$ are

the x and y (transverse) electric field components at the image and object scene, respectively. As Jones vectors have two components, and the Jones matrix four, the linear system of equations is underconstrained. A simple workaround for this problem is to use two different and well-chosen object polarization states, to obtain as much equations as unknowns:

$$\begin{pmatrix} E_{x,i,1} & E_{x,i,2} \\ E_{y,i,1} & E_{y,i,2} \end{pmatrix} = \begin{pmatrix} J_{xx} & J_{xy} \\ J_{yx} & J_{yy} \end{pmatrix} \times \begin{pmatrix} E_{x,o,1} & E_{x,o,2} \\ E_{y,o,1} & E_{y,o,2} \end{pmatrix}. \tag{4.3}$$

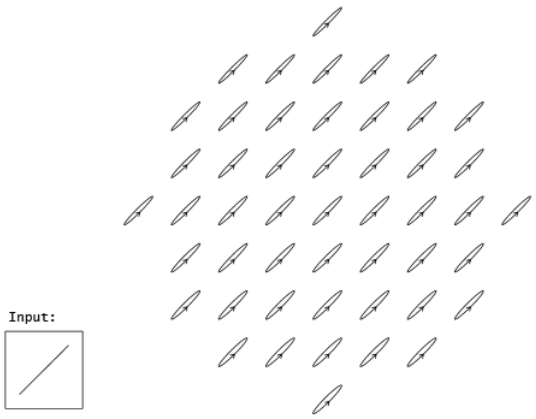

Figure 4.2 – **Polarization pupil map at the image**. Example with linear polarization at +45° and $\lambda = 780$ nm. The sampling is 9×9. The ellipticity shows the impact of the telescope on the polarization state.

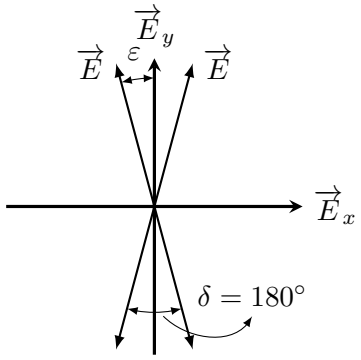

Figure 4.3 – **180° phase shift between the electric field components**. Example with linear vertical polarization. The cause is a sign reversal of the x-component. ε represents an infinitely small deviation from the vertical polarization state.

Linearly polarized light at +45° and −45° is used as the first and second set of data, respectively. There is not just one suitable combination of datasets, but some combinations aren't appropriate for modeling changes in light amplitude and phase. For instance, using both horizontal and vertical polarization states would not work, as the phase shift isn't defined in these cases. Moreover, an abrupt phase jump of 180° occurs when the polarization state shifts from nearly vertical (or horizontal) to nearly vertical (or horizontal) with a change of sign of one electric field component, with the vertical (or horizontal) polarization state being the limit case.

This 180° phase shift in value follows directly from Euler's identity. Considering the general expression of the Jones vector written in polar form, a sign reversal leads to:

$$\begin{pmatrix} E_x \\ E_y \end{pmatrix} = \begin{pmatrix} E_{x0}e^{i\varphi_x} \\ E_{y0}e^{i\varphi_y} \end{pmatrix} \quad \Rightarrow \quad \begin{cases} \begin{pmatrix} E_x \\ E_y \end{pmatrix} = \begin{pmatrix} -E_{x0}e^{i\varphi_x} \\ E_{y0}e^{i\varphi_y} \end{pmatrix} = \begin{pmatrix} E_{x0}e^{i(\varphi_x+\pi)} \\ E_{y0}e^{i\varphi_y} \end{pmatrix} & \text{if} \quad E_x \to -E_x, \\ \begin{pmatrix} E_x \\ E_y \end{pmatrix} = \begin{pmatrix} E_{x0}e^{i\varphi_x} \\ -E_{y0}e^{i\varphi_y} \end{pmatrix} = \begin{pmatrix} E_{x0}e^{i\varphi_x} \\ E_{y0}e^{i(\varphi_y+\pi)} \end{pmatrix} & \text{if} \quad E_y \to -E_y, \end{cases} \tag{4.4}$$

and the phase shift δ writes

$$\delta = \varphi_y - \varphi_x \qquad \Rightarrow \qquad \begin{cases} \delta = \varphi_y - \varphi_x - \pi & \text{if} \quad E_x \to -E_x, \\ \delta = \varphi_y - \varphi_x + \pi & \text{if} \quad E_y \to -E_y. \end{cases} \tag{4.5}$$

Eventually, the solution of Equation 4.3 is determined algebraically, yielding the Jones matrix coefficients:

$$\begin{pmatrix} E_{x,i,1} & E_{x,i,2} \\ E_{y,i,1} & E_{y,i,2} \end{pmatrix} \times \begin{pmatrix} E_{x,o,1} & E_{x,o,2} \\ E_{y,o,1} & E_{y,o,2} \end{pmatrix}^{-1} = \begin{pmatrix} J_{xx} & J_{xy} \\ J_{yx} & J_{yy} \end{pmatrix}. \tag{4.6}$$

It is worth noting that in order to determine the coefficients of the Jones matrix, it is necessary to know the absolute phase of the transverse electric and magnetic modes. Therefore, a reference must be chosen since only the phase difference between the components is known. $\varphi_x = 0$ is chosen as the reference, and as a consequence[1], $\delta = \varphi_x - \varphi_y = -\varphi_y$.

The same procedure can be applied to deduce the Jones matrix of each optical element, as the state of polarization can be retrieved anywhere in the telescope.

4.1.1 Jones pupil matrix of the telescope

Jones pupil matrices describe the change of polarization state in amplitude A and phase φ across the optical system, in function of the pupil coordinates (P_x, P_y) and the wavelength λ, using the Jones matrix formalism. They therefore have the same size as classical Jones matrices introduced in Chapter 2.

$$\begin{aligned} \mathbf{J} &= \begin{pmatrix} J_{xx}(P_x, P_y, \lambda) & J_{xy}(P_x, P_y, \lambda) \\ J_{yx}(P_x, P_y, \lambda) & J_{yy}(P_x, P_y, \lambda) \end{pmatrix} \\ &= \begin{pmatrix} A_{xx}(P_x, P_y, \lambda) e^{i\varphi_{xx}(P_x, P_y, \lambda)} & A_{xy}(P_x, P_y, \lambda) e^{i\varphi_{xy}(P_x, P_y, \lambda)} \\ A_{yx}(P_x, P_y, \lambda) e^{i\varphi_{yx}(P_x, P_y, \lambda)} & A_{yy}(P_x, P_y, \lambda) e^{i\varphi_{yy}(P_x, P_y, \lambda)} \end{pmatrix}. \end{aligned} \tag{4.7}$$

A_{xx} and A_{yy} represent the transmission for x- and y-polarized light, respectively. On the other hand, A_{xy} and A_{yx} denote the amplitude of y-polarized light converted to x-polarized light, and vice versa. In the same way, φ_{xx} and φ_{yy} represent the phase of x- and y-polarized light, respectively, while φ_{xy} and φ_{yx} give the phase of y-polarized light converted to x-polarized light, and vice versa (Anche et al., 2023; Chipman et al., 2015). All these parameters depend on the pupil coordinates and wavelength.

Polarization aberrations

Polarization aberrations (PA) were introduced by Russell A. Chipman in 1987, and defined as the variation of the amplitude, phase and polarization of an optical wavefront across the pupil of an optical system and the dependence of these variations on wavelength and object coordinate (Chipman, 1987).

[1] Following the convention of *Ansys Zemax OpticStudio*.

In an ideal optical system, without any *polarization aberrations*, the Jones pupil matrix would be the identity matrix for each set of pupil coordinates (Zhang et al., 2007). However, the coatings applied on the mirrors and the angles of incidence of light, making mirrors act as retarders, change the game and generate polarization aberrations. As stated by the Fresnel equations, *obliquely incident light on an optical surface will give rise to different variations in amplitude and phase between the orthogonal components of polarization, which is the main cause of polarization aberrations* (He et al., 2017). This is the reason why the third mirror M_3 is the primary cause of polarization aberrations.

The Jones pupil matrices of the telescope for $\lambda = 780$ nm are given in Figures 4.4 and 4.5.

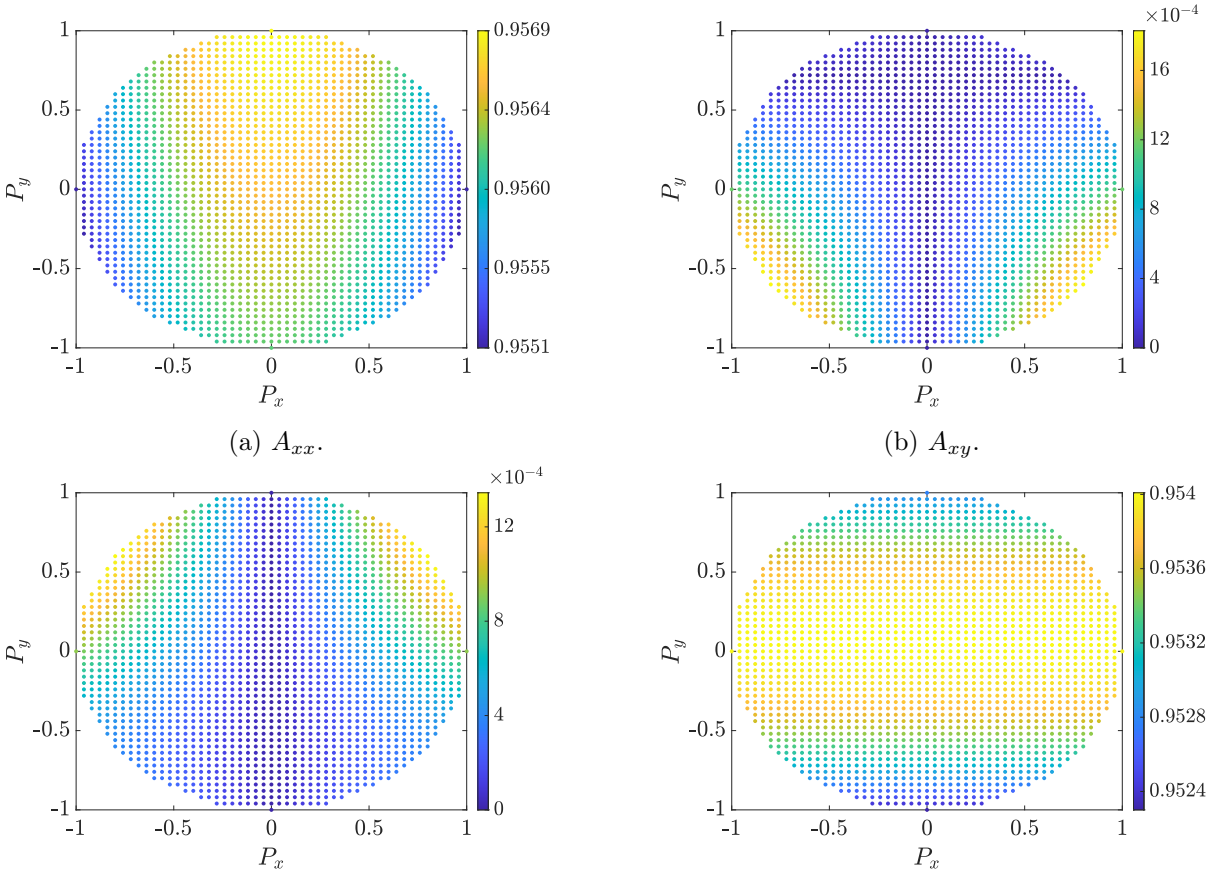

(a) A_{xx}. (b) A_{xy}.

(c) A_{yx}. (d) A_{yy}.

Figure 4.4 – **Amplitude coefficients of the Jones pupil matrices for $\lambda = 780$ nm.**

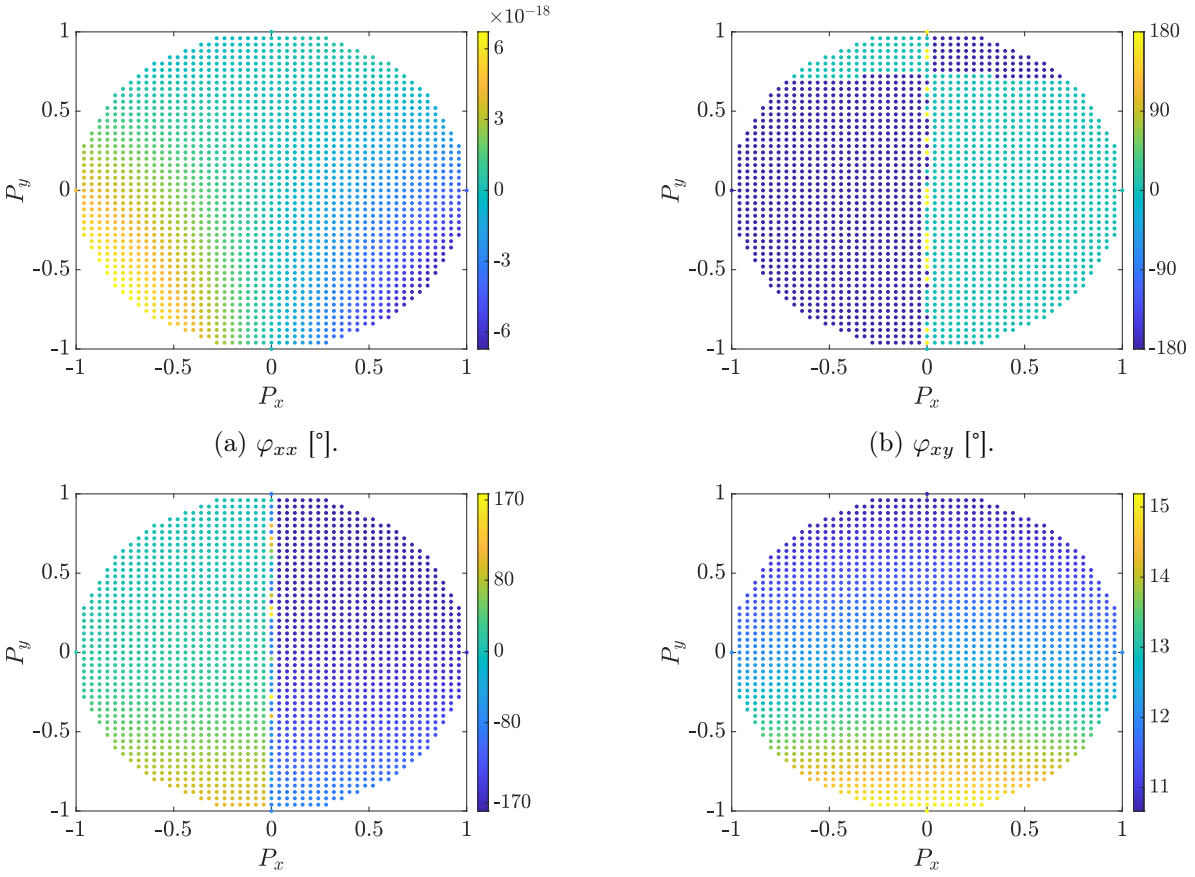

(a) φ_{xx} [°]. (b) φ_{xy} [°].

(c) φ_{yx} [°]. (d) φ_{yy} [°].

Figure 4.5 – **Phase coefficients of the Jones pupil matrices for $\lambda = 780$ nm**. Phase discontinuities of 180° in φ_{xy} and φ_{yx} are caused by a change of sign in the amplitude of one electric field component (see Figure 4.3).

Figure 4.4 shows that the cross-coupled polarizations A_{xy} and A_{yx} are very small and negligible with respect to the transmitted A_{xx} and A_{yy} polarizations. As a consequence, the main impact is the phase shift between the orthogonal components[2], accompanied by losses due to reflections on the mirrors, resulting in an amplitude of less than unity for A_{xx} and A_{yy}. The choice of reference made previously for δ yields $\varphi_{xx} = 0$ everywhere on the pupil, and consequently φ_{yy} is an image of the phase shift as $\varphi_{yy} = -\delta$. The Jones pupil matrices for $\lambda = 685$ nm and $\lambda = 1550$ nm can be found in Appendix B.

4.1.2 Jones matrix of the telescope

Equation 4.7 is the mathematical representation of the Jones matrix at each set of pupil coordinates. The final Jones matrix of the system, independent of the pupil coordinates, requires to take into account the interference of the light rays of each set of pupil coordinates, to eliminate this dependence. The aim is the transition from a Jones matrix that depends on the pupil coordinates (P_x, P_y) and wavelength λ to a pupil-coordinate-independent Jones matrix that still retains dependence on wavelength:

[2] According to the choice made previously for the absolute phases of the components.

$$J(P_x, P_y, \lambda) = \begin{pmatrix} J_{xx}(P_x, P_y, \lambda) & J_{xy}(P_x, P_y, \lambda) \\ J_{yx}(P_x, P_y, \lambda) & J_{yy}(P_x, P_y, \lambda) \end{pmatrix} \quad \Rightarrow \quad J(\lambda) = \begin{pmatrix} J_{xx}(\lambda) & J_{xy}(\lambda) \\ J_{yx}(\lambda) & J_{yy}(\lambda) \end{pmatrix}. \tag{4.8}$$

The amplitude and phase components of J_{xx}, J_{xy}, J_{yx} and J_{yy} are found by averaging the real and imaginary parts of the Jones pupil matrix to combine the waves, thus taking into account the interferences, yielding the final wave. For each term of the Jones matrix, one has

$$\Re(J(\lambda)) = \frac{1}{N} \sum_{(P_x,\ P_y)} \Re(J(P_x, P_y, \lambda)), \tag{4.9}$$

$$\Im(J(\lambda)) = \frac{1}{N} \sum_{(P_x,\ P_y)} \Im(J(P_x, P_y, \lambda)), \tag{4.10}$$

where N is the number of samples. Conversion from Cartesian coordinates to polar coordinates allows retrieving the amplitude and phase terms of each component. Knowing the incoming polarization state of the photon, the outgoing polarization state is now deduced from the Jones calculus with the wavelength-dependent Jones matrix of the telescope.

Figure 4.6 shows the evolution of the Jones matrix coefficients J_{xx}, J_{xy}, J_{yx} and J_{yy} in function of the wavelength λ. Polarization aberrations cause the deviation from the identity matrix. Indeed, Figure 4.6a shows the evolution of the equivalent reflectance coefficient of the telescope for the x-component of the polarization, and Figure 4.6d for the y-component. The phase of the latter corresponds to the opposite of the phase shift, given the reference of a null phase for the x-component. Numerical errors in J_{xy} and J_{yx} cause phases[3] which have no physical meaning given the zero amplitude. These amplitudes are zero as the cross-coupled components of the Jones pupil matrix were.

4.2 Performances

In the case of a quantum optical communication antenna, the performances of the antenna, i.e. of the telescope, directly depend on the ability to maintain the initial polarization state such that when the information is observed at the detector, it is not biased. Given the phase shifts between the orthogonal components of the polarization generated mainly by the third mirror, the Jones matrix is not unitary, as shown by Figure 4.6, which inevitably has an impact on the telescope's performances. The characterization of the telescope's performances is based on the *polarization extinction ratio*, which must meet the objectives set for the three wavelengths (QKD, beacon and telecommunication).

4.2.1 Polarization extinction ratio

Polarization extinction ratio

The *polarization extinction ratio* (PER) is the ratio of the optical powers of the perpendicular polarizations, known as the *transverse electric* and *transverse magnetic* modes. It is therefore a measure of the quality of the linear polarization of light in an optical system.

[3]Large variations in the phase of J_{yx} are due to frequent variations in the sign of the real part, as a complex number's phase changes by 180° when the sign of the real part reverses.

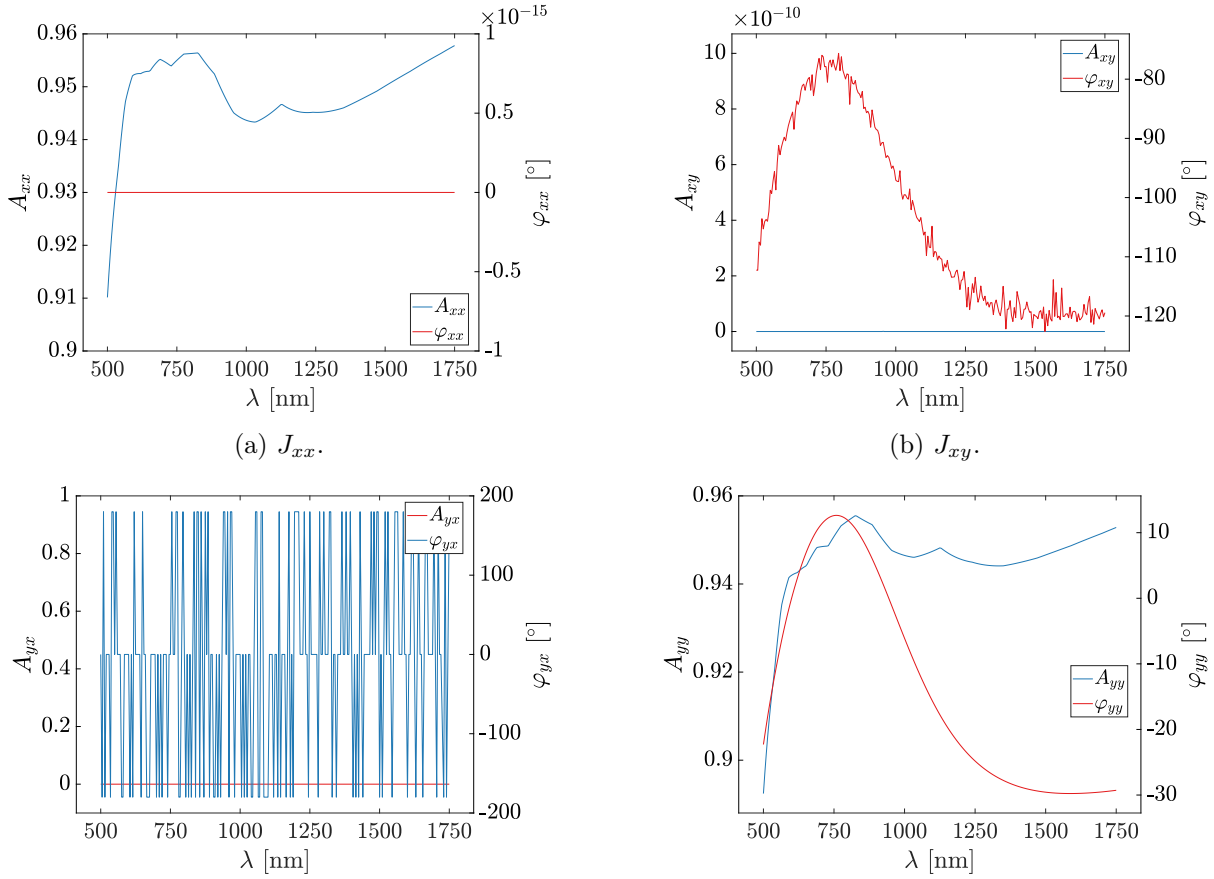

(a) J_{xx}. (b) J_{xy}.

(c) J_{yx}. (d) J_{yy}.

Figure 4.6 – **Amplitudes and phases of the Jones matrix coefficients in function of wavelength.**

The procedure to calculate the polarization extinction ratio relies on the Jones formalism[4], by first determining the polarization state at the image knowing the object scene polarization state, as described above:

$$\mathbf{E}_\mathrm{i} = \mathbf{J} \times \mathbf{E}_\mathrm{o}. \tag{4.11}$$

The phases of the transverse components E_x and E_y are

$$\varphi_x = \tan^{-1}\left(\frac{\Im(E_x)}{\Re(E_x)}\right), \tag{4.12}$$

$$\varphi_y = \tan^{-1}\left(\frac{\Im(E_y)}{\Re(E_y)}\right), \tag{4.13}$$

and the auxiliary angle α writes

$$\alpha = \tan^{-1}\left(\frac{E_y}{E_x}\right) = \tan^{-1}\left(\frac{\sqrt{\Re(E_y)^2 + \Im(E_y)^2}}{\sqrt{\Re(E_x)^2 + \Im(E_x)^2}}\right). \tag{4.14}$$

[4]This is not the only way to proceed, as one could also start from the definition of the PER given above. This would, however, not give any information relative to the phases, and thus not allow to determine the phase shift to compensate for each wavelength.

The ellipticity angle derives from Equation 2.39:

$$\chi = \frac{1}{2}\sin^{-1}\left(\sin 2\alpha \sin\delta\right), \tag{4.15}$$

and eventually, the polarization extinction ratio can be written in function of the ellipticity angle (Wu et al., 2020):

$$PER = \frac{1}{\tan^2\chi}. \tag{4.16}$$

In order to ensure the accuracy of the PER values obtained as a function of wavelength, and more particularly at the wavelengths of interest, a convergence analysis is carried out as a function of spatial sampling S on the polarization pupil map, from which all the data useful for Jones's calculations are taken. In pursuit of this goal, and anticipating on the values of the PER[5], the relative error η_i between two values of the PER, at samplings S_i and S_{i+1}, is defined as

$$\eta_i = \frac{PER(\lambda)_{S_{i+1}} - PER(\lambda)_{S_i}}{PER(\lambda)_{S_i}}. \tag{4.17}$$

Figure 4.7 shows that the relative error is low even at low sampling. For the sake of precision, an acceptable relative error of 0.01% is chosen, which corresponds to a sampling of 49×49.

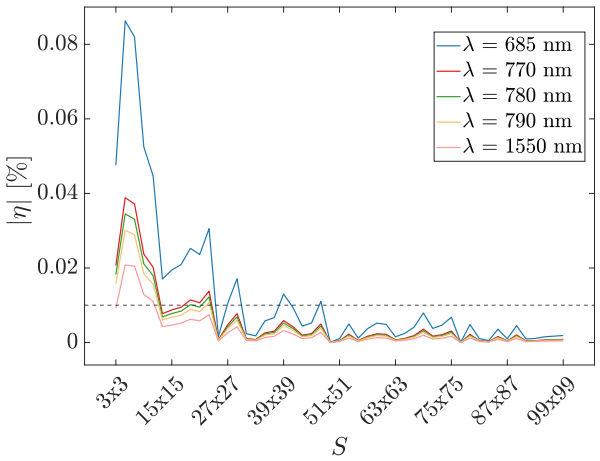

Figure 4.7 – **Convergence analysis of the PER in function of the spatial sampling**. Polarization is linear at +45°. The acceptable relative error is shown by the dotted line.

The PER at convergence are given in Table 4.1.

4.2.2 PER sensitivity to polarization orientation

Figure 4.8 shows the variation of the PER as a function of the polarization orientation supplied at the object scene ψ_o, for the wavelengths of interest. The results show that the PER is too low as compared to the targeted values to guarantee that the PER objectives will be achieved for all types of linear

[5]The worst-case scenario for the PER is ±45° polarization, as will be shown later. The convergence analysis is done for this type of polarization.

Table 4.1 – **Polarization extinction ratios.** Objectives values are dictated by the SpeQtral company.

Wavelength	Telescope PER	Targeted PER
685 nm	130 : 1	200 : 1
770 nm	82 : 1	1000 : 1
780 nm	84 : 1	1000 : 1
790 nm	88 : 1	1000 : 1
1550 nm	14 : 1	200 : 1

polarization, due to too large phase shifts between the orthogonal components of polarization. The worst case corresponds to $\psi_o = \pm 45°$ polarization, as identified from Figure 4.8, while horizontal and vertical polarizations have an infinite PER. Consequently, $\psi_o = \pm 45°$ will be considered the worst-case scenario for the remainder of this project, which is in accordance with the work of Arteaga-Díaz et al. (2020) on polarization degradation induced by reflection at an angle of incidence (AOI) of 45°.

These results were expected as $\psi_o = \pm 45°$ correspond to the case of equal amplitudes in value for both electric field components. The importance of the phase shift is therefore maximal in this case, while it becomes less and less noticeable as the value of one of the components tends towards zero. Independently of δ, by Equation 4.15, the ellipticity is minimized for $\psi = k\pi/2$ ($k \in \mathbb{Z}$), and maximized if $\psi = k\pi/4$ ($k \in \mathbb{Z}$). Consequently, as dictated by Equation 4.16, the PER is minimized when the ellipticity is maximized, and vice versa.

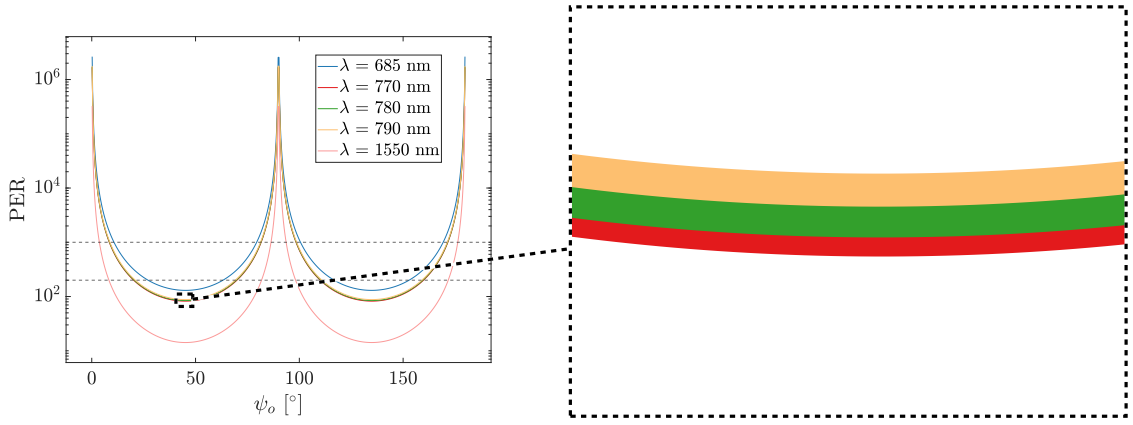

(a) PER in function ψ_o.

(b) Zoom on the QKD wavelength band. Curves almost merge due to the small difference in phase shift.

Figure 4.8 – **PER in function of linear polarization orientation at the object scene**. Infinite PER corresponding to horizontal and vertical polarization have been omitted for the ease of visualization. Targeted PER are represented by the dotted lines.

The other parameter defining the PER is, as previously introduced, the phase shift δ. For a given orientation of the linear polarization, increasing values of χ in the interval $0 \leq \chi \leq \pi/4$ will gradually transform the polarization ellipse from a straight line (linear polarization) for $\chi = 0$ to a circle (circular polarization), at $\chi = \pi/4$. This increase in the phase shift decreases the PER, up to $\delta = \pi/2$, given the increase of the ellipticity angle. The ellipticity angle reaches its maximum value at this point. If δ continues to increase, the minor and major axes of the polarization ellipse reverse, and further value

increases of δ decrease the ellipticity, the latter being defined with respect to the minor and major axes of the ellipse. The PER increases again as the ellipticity now decreases. The same explanations are valid for decreasing values of δ, which lead to negative values for ellipticity with a minimum at $\chi = -\pi/4$ (circular polarization).

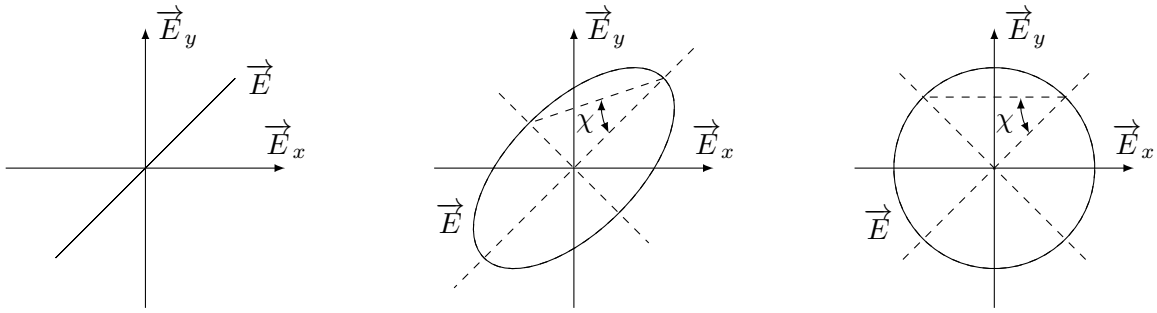

(a) $\delta = 0$, $\chi = 0$. (b) $0 < \delta < \pi/2$, $0 < \chi < \pi/4$. (c) $\delta = \pi/2$, $\chi = \pi/4$.

Figure 4.9 – **Ellipticity angle**. Impact of the phase shift δ on the ellipticity angle χ.

4.2.3 Wavelength-dependent parameters

Polarization orientation

Figure 4.10 shows the wavelength-dependent impact of polarization aberrations, leading to slight variations in the polarization orientation ψ. More precisely, as the cross-coupled polarization is small but non-zero, a conversion from x to y polarization takes place, and vice versa, thus causing small variations in ψ. At the wavelengths of interest, these variations are of the order of a tenth of a degree in the worst-case scenario.

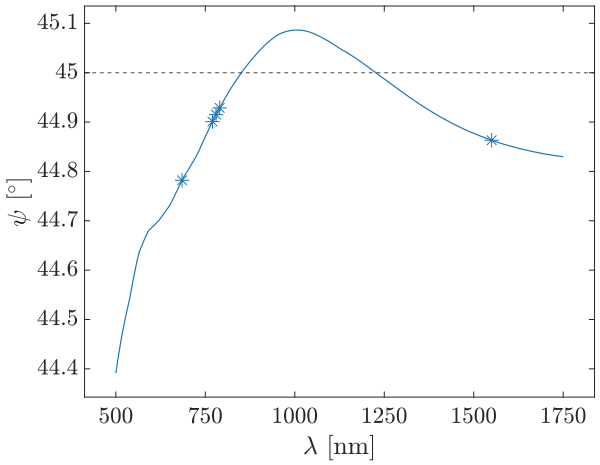

Figure 4.10 – **Polarization orientation at the image in function of wavelength**. Initial polarization state is 45°. Asterisks show the phase shift at the wavelengths of interest.

It is important to note that there is no guarantee that $\psi = \pm 45°$ is the type of polarization with the largest variations in orientation. Indeed, Equation 2.38 indicates that ψ depends on the phase shift, and on the ratio of the electric field components amplitudes. As these parameters are wavelength-dependent, each wavelength can present different orientation changes for different polarization types at the object scene. However, since the objectives are expressed in terms of PER, which is minimal for $\psi = \pm 45°$, these are the provided results for illustration purposes.

Phase shift

Fresnel's equations show that the reflection coefficients for transverse electric and transverse magnetic polarization depend on the refractive index of the medium before reflection and on the medium generating the reflection. Since refractive indices depend on the wavelength, the phase shift between the transverse components also depends on the wavelength (Clarke, 2010). Figure 4.11 illustrates the variation of the phase shift in function of the wavelength, which is independent of the type of polarization[6].

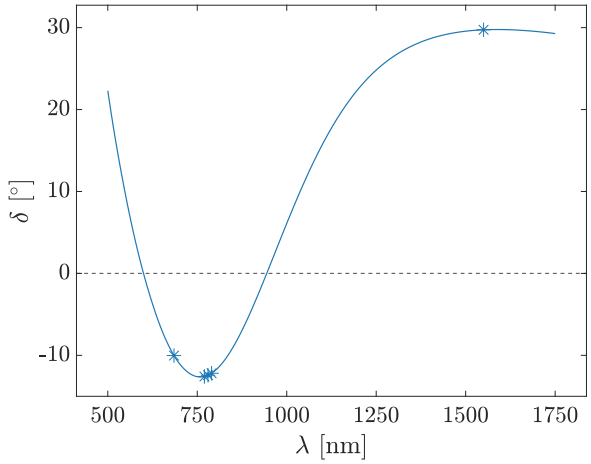

Figure 4.11 – **Phase shift in function of the wavelength**.

In compliance with Figure 4.9, the polarization of the incoming photon is transformed from linear to elliptical, with increasing ellipticity for an increasing phase shift in absolute value. At two wavelengths, however, the phase shift is zero, and consequently is the ellipticity.

Polarization extinction ratio

The two wavelengths of zero phase shift are wavelengths corresponding to maximum PER, as a consequence of Equations (4.15) and (4.16), resulting in a maintained polarization state. As can be observed in Figures 4.11 and 4.12, the two peaks are not located at the desired wavelengths, and the PER at the relevant wavelengths for this project do not meet the objectives. In the following chapter (Chapter 5), it will be necessary to align the maximum PER values with the desired wavelengths, or to at least achieve the objectives at these wavelengths, by correction of the phase shift.

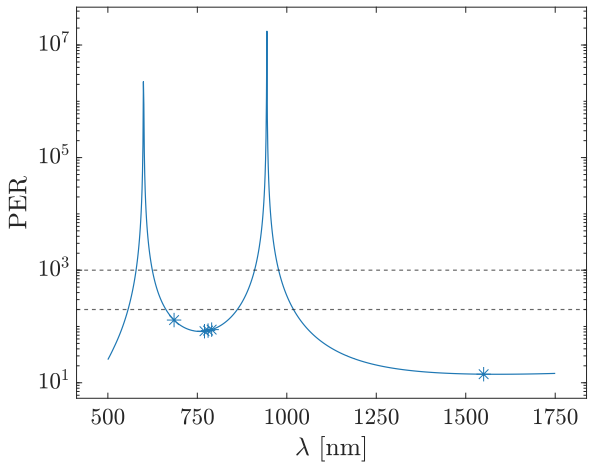

Figure 4.12 – **PER in function of the wavelength for ±45° polarization orientation**. Objectives values are represented by the dotted lines. A zero-degree phase shift corresponds to an infinite PER.

[6]Excluding the special cases of horizontal and vertical polarizations. The concept of phase shift does not exist due to the null component of the electric field.

Part IV

Polarization-maintaining telescope design

Chapter 5

Polarization-maintaining design

The study of the impact of the telescope on the polarization of the light, conducted in Chapter 4, has provided valuable insights for the development of solutions aimed at correcting this impact. Now that the retardance between the orthogonal components of the electric field composing the light has been characterized, as a function of wavelength, it is possible to explore solutions to compensate this retardance at the desired wavelengths. Hence, research logically turns towards means of modifying the existing telescope design, which may also involve the addition of new elements, to reach the objectives.

5.1 State of the art

There are several possible solutions to correct phase delays between the components of polarization. Basically, research is focusing either on ways of inducing no phase shift between the components, or on ways of compensating for the phase shifts induced by the telescope. In the first case, given that the telescope inevitably induces phase delays at the wavelengths corresponding to the application, the only possibility is to modify the telescope design. This may involve geometric modifications, as modifying the telescope configuration for instance, to avoid using the third mirror M_3, which given its orientation, is the main culprit of polarization degradation.

Another possibility is to modify the coatings applied on the mirrors. By rigorously choosing the type of coatings and the thicknesses of the layers, it is possible to induce an optical path difference (OPD) corresponding to the compensation of phase delays. This possibility of using *phase retarding optical coatings* has been studied in literature, and Fabricius and Hansen (2008) illustrated the design methodology using the optimization of a merit function.

In the second case where research investigates the possibility to compensate the induced phase shifts, one possibility is to make use of the principle of birefringence, which enables to induce phase shifts between orthogonal components of light. Miller et al. (2022) illustrated the feasibility of this solution by using several birefringent elements, each of which has three variable parameters: the thickness, the orientation of the fast axis, and the choice of material. Optimization of a merit function, based on the difference between the identity matrix and the Mueller matrix of the optical system[1], was performed numerically using a multivariable merit function optimization function.

[1] As light was not fully polarized, the Jones formalism was not suitable and one had to use the more general Mueller formalism.

Still based on the principle of birefringence, liquid crystals can be used to correct phase delays. These have the particularity of having a birefringence that can be controlled by applying an electric field between two electrodes:

$$\Delta\varphi(\lambda, \Delta V) = \frac{2\pi}{\lambda} d\Delta n(\lambda, \Delta V). \tag{5.1}$$

The induced phase shift can be controlled by varying the electric field, and it is then possible to freely choose which, if not several, wavelength to optimize. This method is, however, more difficult to implement, as it requires an external current source, as well as electrodes that are transparent to the wavelengths whose phase shift is to be corrected.

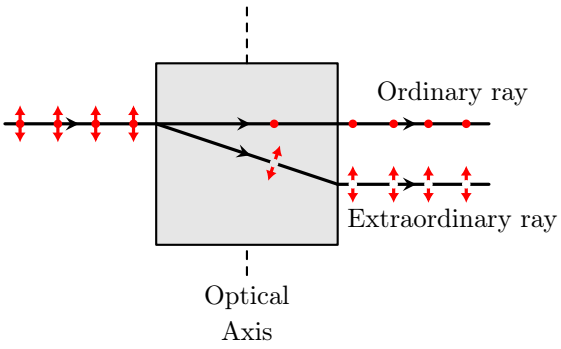

Figure 5.1 – **Birefringence.** A different propagation direction and optical axis orientation yields different phase velocities for the ordinary and extraordinary rays. *Adapted from Tsagkaropoulos (2021).*

As the design of the telescope is fixed, and in order to be versatile with respect to future missions that could make use of different wavelengths, the solution involving a modification of the coatings is not considered for this work, but was nevertheless studied by AMOS. Retardation plates will thus be used to simultaneously compensate several wavelengths.

5.2 Light propagation in crystals

The propagation of electromagnetic, monochromatic plane waves in anisotropic materials can be described mathematically by using Maxwell's equations combined with constitutive relations, as described in Chapter 2. Full developments can be found in the work of Born and Wolf (1999), but the developments directly useful to the physical understanding of light propagation are the focus of attention.

Fresnel's equation of wave normals describes light propagation of a monochromatic plane wave in an anisotropic medium:

$$s_x^2 \left(v_p^2 - v_y^2\right)\left(v_p^2 - v_z^2\right) + s_y^2 \left(v_p^2 - v_z^2\right)\left(v_p^2 - v_x^2\right) + s_z^2 \left(v_p^2 - v_x^2\right)\left(v_p^2 - v_y^2\right) = 0, \tag{5.2}$$

with $\overrightarrow{s} = (s_x, s_y, s_z)$ the wave normal vector, v_p the phase velocity, being function of the speed of light c and the refractive index of the medium n:

$$v_p = \frac{c}{n}. \tag{5.3}$$

Fresnel's equation also depends on the *principal velocities of propagation*, v_x, v_y and v_z:

$$v_x = \frac{c}{\sqrt{\mu\varepsilon_x}}, \qquad v_y = \frac{c}{\sqrt{\mu\varepsilon_y}}, \qquad v_z = \frac{c}{\sqrt{\mu\varepsilon_z}}, \tag{5.4}$$

with $\varepsilon_x, \varepsilon_y$ and ε_z the *principal dielectric constants*, or *principal permittivities*, and μ the magnetic permeability. In the particular case of a uniaxial crystal[2], with its optical axis oriented in the z

[2] As most optical applications make use of uniaxial crystals, the discussion is limited to the propagation of plane waves

direction, $v_x = v_y$. By writing v_o for this velocity, and $v_e = v_z$, for the sake of terminology, the expression above simplifies to

$$\left(v_p^2 - v_o^2\right)\left[\left(s_x^2 + s_y^2\right)\left(v_p^2 - v_e^2\right) + s_z^2\left(v_p^2 - v_o^2\right)\right] = 0. \tag{5.5}$$

The change of terminology is motivated by the intention to be consistent with the usual terminology, using *ordinary* and *extraordinary* terms, hence the suffixes o and e. These concepts will be clarified hereafter. Writing ϑ for the angle between the wave normal s and the z-axis, and knowing that $s_x^2 + s_y^2 + s_z^2 = 1$, one has

$$s_z^2 = \cos^2\vartheta, \tag{5.6}$$

$$s_x^2 + s_y^2 = \sin^2\vartheta, \tag{5.7}$$

and Equation 5.5 becomes

$$\left(v_p^2 - v_o^2\right)\left[\sin^2\vartheta\left(v_p^2 - v_e^2\right) + \cos^2\vartheta\left(v_p^2 - v_o^2\right)\right] = 0. \tag{5.8}$$

The roots of this equation, written v_{p1} and v_{p2}, are:

$$v_{p1} = v_o, \tag{5.9}$$

$$v_{p2} = \sqrt{v_o^2\cos^2\vartheta + v_e^2\sin^2\vartheta}. \tag{5.10}$$

These roots show that the normal surface consists of two shells: a sphere of radius v_o and an ovaloid. Thus, light is split into two types of waves depending on the direction of the normal to the wave surface (wavefront) at that point. One of these waves is called the *ordinary wave*, whose propagation velocity is independent of the direction of propagation. The other is the *extraordinary wave*, whose velocity depends on the angle between the direction of the wave normal and the optical axis of the crystal. If $\vartheta = 0$, both phase velocities are equal and the wave normal lies in the direction of the optical axis.

Two cases are then possible. If $v_o > v_e$, the extraordinary wave travels slower than the ordinary wave. These types of crystals are called *positive uniaxial crystals*. On the other hand, if $v_o < v_e$, the extraordinary wave travels faster than the ordinary wave, and one speaks of *negative uniaxial crystals*.

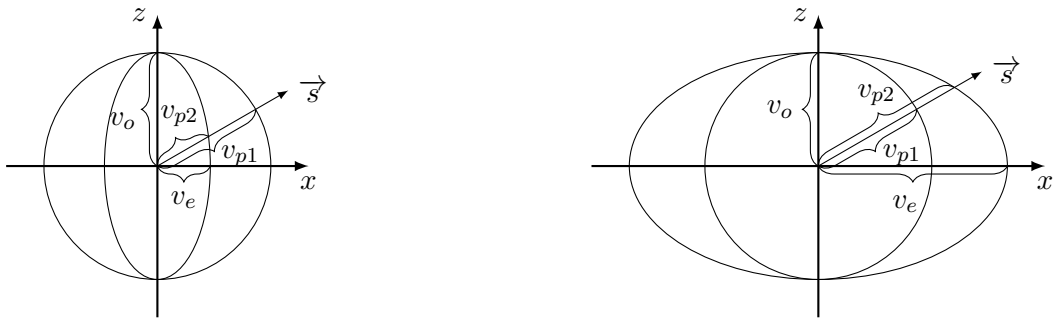

(a) Positive uniaxial crystal : $v_e < v_o$.

(b) Negative uniaxial crystal : $v_e > v_o$.

Figure 5.2 – **Ellipsoid of wave normals of uniaxial crystals**. *Adapted from Born and Wolf (1999).*

in these types of crystals.

5.3 Arrangement of retardation plates inside the telescope

The use of *birefringence*, as illustrated above, makes it possible to induce a phase shift between the orthogonal components of polarization, due to their different refractive indices, and so propagation velocities, in a crystal. However, the impact of one or more retardation plates will vary depending on their placement within the telescope, and the PER will be affected. In order to achieve the best possible results while minimizing polarization aberrations, the crystals are placed in a collimated beam at the output of the telescope, after the pupil deformed mirror (Arteaga-Díaz et al., 2020). The number of retardation plates to use, their orientations, and their thicknesses, are a priori unknown. The detailed study that follows examines these parameters to determine the ideal combination for achieving the objectives.

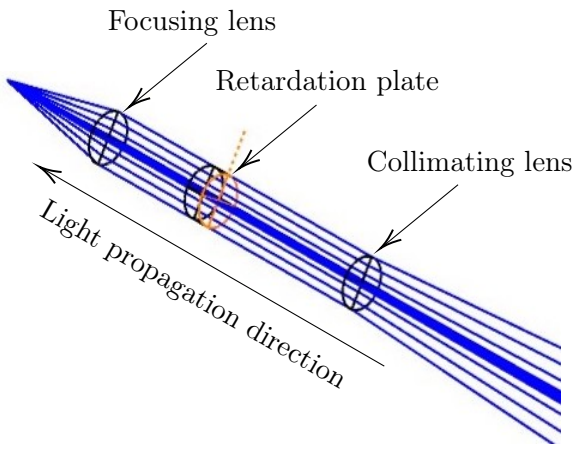

Figure 5.3 – **Arrangement of the retardation plates in the telescope.** Example with one plate. The dotted line represents the optical axis, and the collimating lens represents the corrector.

5.4 Polarization extinction ratio optimization

5.4.1 Optimization using one crystal

The retardance induced between the orthogonal components of polarization due to the propagation of light through a single crystal of thickness d and birefringence Δn is expressed by:

$$\Delta\varphi(\lambda) = \frac{2\pi}{\lambda} d\Delta n(\lambda). \tag{5.11}$$

The induced phase shift is a function of the wavelength, and depends on the type of crystal. The choice of the latter is free, but it is still important to ensure that transparency at the useful wavelengths is high. Moreover, the crystal must remain financially affordable and manufacturable with sufficient ease. A good candidate respecting these conditions is magnesium fluoride (MgF_2).

In order to determine the thickness required to correct the phase shift, a choice must be made regarding the wavelength for which the PER must be optimized. This stems from the fact that crystals do not exhibit sufficiently different birefringences at different wavelengths, with the consequence that it is not possible to induce significantly different phase shifts at different wavelengths. The dispersion curve of the crystal does

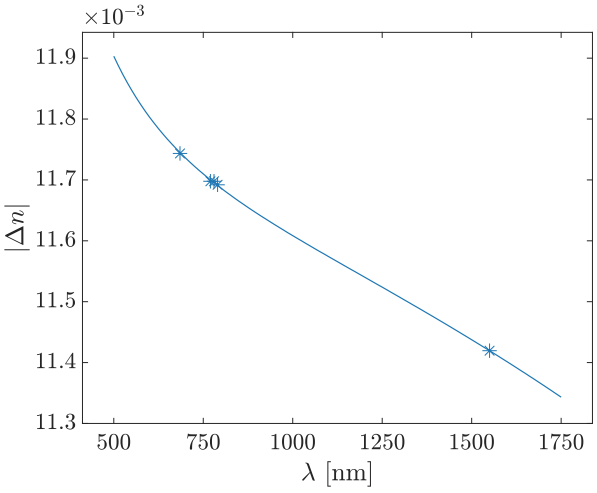

Figure 5.4 – **Birefringent properties of MgF_2.** Absolute birefringence is considered as negative values correspond to a perpendicular orientation of the crystal axis.

thus not allow to match the phase retardance of
the mirrors for each wavelength.

As one wants to correct the phase shift, the crystal must induce a phase shift opposite to the one induced by the telescope:

$$-\delta(\lambda) = \frac{2\pi}{\lambda} d\Delta n(\lambda), \tag{5.12}$$

with $\delta(\lambda)$ the telescope-induced phase shift. The thickness writes:

$$d = -\frac{\delta(\lambda)\lambda}{2\pi\Delta n(\lambda)}. \tag{5.13}$$

Optimization at the three main wavelengths requires the thicknesses given in Table 5.1. It is possible to obtain negative values for the thickness when solving Equation 5.13. This means that the *slow* axis and *fast* axis orientations must be inverted, corresponding to a reversal between the ordinary and extraordinary refractive index. According to the *Ansys Zemax OpticStudio* model of the telescope, a positive value means that the optical axis is directed along the x-direction in the global coordinate reference frame, while a negative value means that the optical axis is along the z-direction. The y-direction corresponds to the propagation direction, and does thus not generate a phase shift.

Table 5.1 – **Required thickness for the crystal in function of the wavelength to optimize.** OA denotes the orientation of the optical axis of the crystal.

λ	d	OA
Beacon	$1.625 \cdot 10^{-3}$ mm	z
QKD	$2.302 \cdot 10^{-3}$ mm	z
Telecommunication	$11.211 \cdot 10^{-3}$ mm	x

The previously made assertion that optimizing more than one wavelength is not possible if the wavelengths are too far apart, in the sense that the phase shift varies too much between the wavelengths, can now be verified. For instance, optimization at the QKD wavelength would require $\Delta n = 0.056$ at the telecommunication wavelength to compensate its phase shift with a given thickness corresponding to the one needed for QKD. This is not feasible as $\Delta n = -0.011$ at the telecommunication wavelength. This value is firstly too low, but secondly, and more importantly, this negative value indicates that it is necessary to have a perpendicular orientation of the crystal's optical axis for both wavelengths, which is impossible since there is only one crystal. This leads us to believe that the use of multiple crystals may allow optimization at multiple wavelengths, and this option will be studied later.

Instead of dealing with very low thicknesses such as those obtained, it is possible to make good use of the property of birefringence to achieve more realistic thicknesses. To this end, two crystals of the same material, but of different thicknesses d_1 and d_2, are used. The fast axis of the first crystal is aligned with the slow axis of the second, and so everything happens as if there was only one crystal whose phase delay is exactly that generated by the crystal whose thickness is equal to the difference in thickness between the two crystals. If $d_2 = d_1 + d$ is the thickness of the thicker crystal with the optical axis oriented according to the solution found by solving Equation 5.13, one has

$$
\begin{aligned}
-\delta(\lambda) &= \frac{2\pi}{\lambda}\Delta n(\lambda)d_1 - \frac{2\pi}{\lambda}\Delta n(\lambda)d_2, && (5.14)\\
&= \frac{2\pi}{\lambda}\Delta n(\lambda)d_1 - \frac{2\pi}{\lambda}\Delta n(\lambda)(d_1 + d), && (5.15)\\
&= -\frac{2\pi}{\lambda}\Delta n(\lambda)d, && (5.16)
\end{aligned}
$$

with the minus sign corresponding to the second crystal as for the sake of the example above of optimization at the QKD wavelength, the optical axis was along the z-direction. Manufacturers of retardation plates also employ this methodology to produce zero-order retardation plates (Edmund Optics, 2024). The evolution of the PER by separately optimizing the three main wavelengths is shown in Figure 5.5, and the corresponding retardance in Figure 5.6.

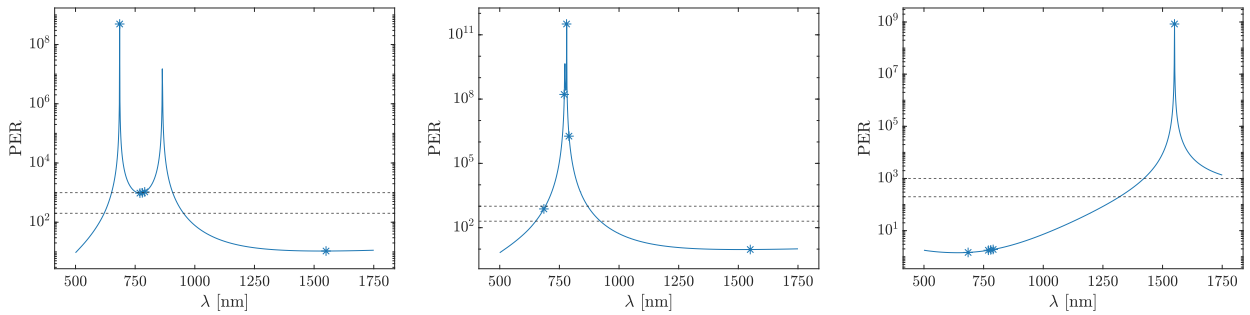

(a) Beacon. (b) QKD. (c) Telecommunication.

Figure 5.5 – **PER in function of wavelength for optimization at the three main wavelengths**. Two peaks are visible for beacon optimization as the phase shift at this wavelength also corresponds to another wavelength.

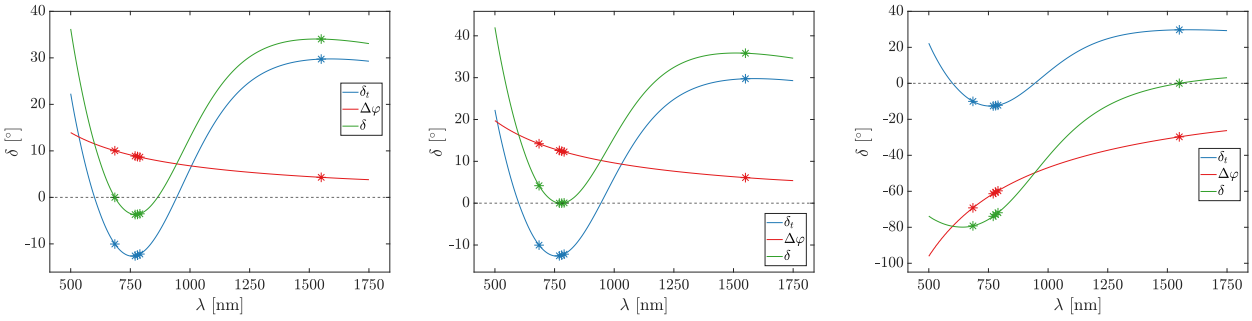

(a) Beacon. (b) QKD. (c) Telecommunication.

Figure 5.6 – **Phase shift in function of wavelength for optimization at the three main wavelengths**. δ_t is the phase shift induced by the telescope, $\Delta\varphi$ the phase shift induced by the crystal, and $\delta = \delta_t + \Delta\varphi$ the resulting phase shift. The latter is the result of optimization at the desired wavelength.

Given that the priority order in achieving the PER objectives states that the QKD wavelength is the most important to optimize, followed by the beacon wavelength, optimizing at the QKD wavelength (Figure 5.5b) or at the beacon wavelength (Figure 5.5a) are the solutions to consider. Unfortunately, due to the considerable differences between the phase shifts at the beacon or QKD wavelengths and

the telecommunication wavelength (see Figure 4.11), good performances at these wavelengths come at the expense of poor performances at the telecommunication wavelength.

High-order solutions

The thicknesses in Table 5.1 lead to a phase shift exactly opposite to that induced by the telescope, δ, and are called *zero-order* solutions. These thicknesses are, however, too thin to be manufactured in practice.

An alternative to address this problem is to consider *high-order* solutions. Introducing a phase shift $-\delta$ is equivalent to the introduction of a phase shift $-\delta + 2k\pi$, with $k \in \mathbb{Z}$ (Crabtree, 2007). This approach allows finding larger thicknesses while inducing in fact the same phase shift. As a consequence, the number of possible thicknesses is infinite. The new equation to be solved to determine the thickness of the crystal and the orientation of its optical axis is therefore

$$-\delta(\lambda) + 2k\pi = \frac{2\pi}{\lambda}\Delta n(\lambda)d, \tag{5.17}$$

and the increase in thickness Δd is proportional to the order k:

$$\Delta d = \frac{(-\delta(\lambda) + 2k\pi)\,\lambda}{2\pi\Delta n(\lambda)} - \left(-\frac{\delta(\lambda)\lambda}{2\pi\Delta n(\lambda)}\right) = \frac{k\lambda}{\Delta n(\lambda)}. \tag{5.18}$$

Solving Equation 5.17 for instance for QKD optimization for different orders gives the results in Table 5.2. The thickness increases with the order, and negative orders have a perpendicular optical axis orientation with respect to positive orders as the phase shift to compensate changes sign for negative orders.

Table 5.2 – **Higher-order solutions for QKD optimization.**

k	0	1	-1	2	-2	3	-3
d [mm]	$2.302 \cdot 10^{-3}$	$6.899 \cdot 10^{-2}$	$6.438 \cdot 10^{-2}$	$1.357 \cdot 10^{-1}$	$1.311 \cdot 10^{-1}$	0.202	0.198
OA	z	z	x	z	x	z	x

Opposite-order solutions have very similar but different thicknesses. Naturally, it directly follows from Equation 5.17 that the thicknesses can only be identical if the phase shift to be corrected is zero, in which case there is only a difference of signs in the thicknesses, i.e. a perpendicular orientation of the optical axes of opposite-order solutions.

Figure 5.7 shows the PER in function of wavelength for QKD optimization of order 1. At the QKD wavelength, the PER is high thanks to the optimization, and another high-PER region appears. Even though the latter has a high PER, this optimization is in fact not suitable as the polarization orientation at these wavelengths is reversed. This is confirmed by Figure 5.8, which shows that in the vicinity of the undesired optimized PER region, the phase shift passes through $\delta = 180°$, meaning that the components are not in-phase anymore. Therefore, when analyzing the performances obtained, it is advisable to remain cautious and always analyze the retardance in addition to the PER when exploring unwanted optimized wavelengths.

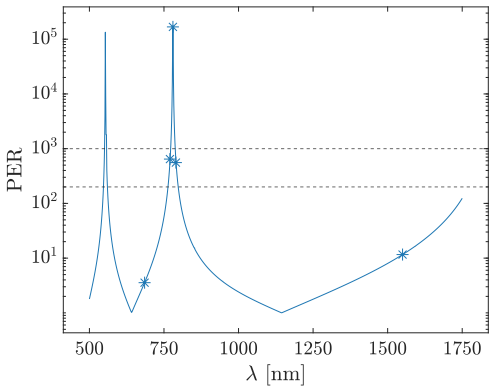

Figure 5.7 – **PER in function of wavelength for first-order QKD optimization.**

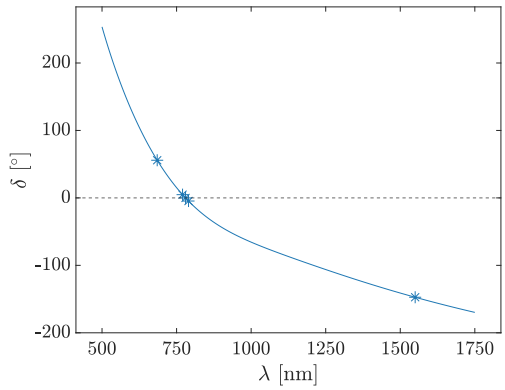

Figure 5.8 – **Phase shift in function of wavelength for first-order QKD optimization.** The phase shift zone passing through 180° is a parasitic optimization.

Moreover, a non-negligible disadvantage of this method is the reduction in the width of the optimized wavelength band. This is the direct consequence of a large variation in the phase shift within the area of interest. The retardance variation directly depends on the derivative of the phase shift induced by the crystal, as the phase shift induced by the telescope is independent of the latter. Mathematically, the derivative of the crystal's phase shift is:

$$\frac{\partial \Delta\varphi}{\partial \lambda} = -\frac{2\pi}{\lambda^2} d\Delta n(\lambda) + \frac{2\pi}{\lambda} d\frac{\partial \Delta n(\lambda)}{\partial \lambda}. \tag{5.19}$$

Small wavelengths thus suffer from high variations of crystal-induced phase shift, and so from high phase shift variations in the whole system, i.e. telescope and crystal together. For a fixed wavelength, increasing the order (increasing the thickness) increases the derivative as it is linearly dependent on the thickness. Therefore, it can be concluded that higher-order solutions have greater phase shift variations (Crabtree, 2007), and consequently smaller optimized bandwidths, simultaneously explaining the increase of the number of high-PER bands. Because of this drawback in terms of bandwidth, higher-order solutions are not considered and the study concentrates on zero-order solutions only.

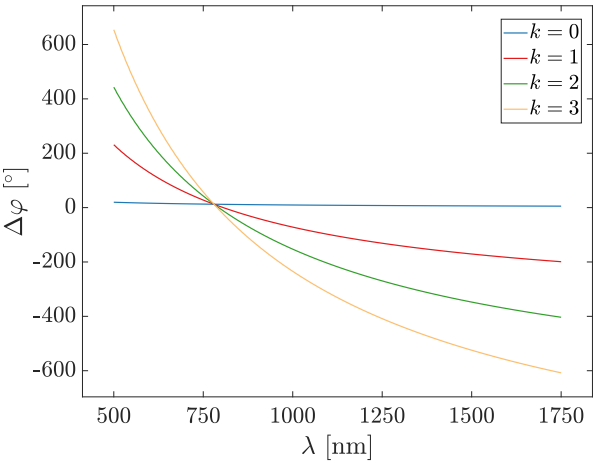

Figure 5.9 – **Crystal-induced phase shift for thicknesses corresponding to QKD optimization.** Non-zero order solutions were shifted by multiples of 360° for the ease of comparison and to have a common intersection at the QKD wavelength.

Tolerance analyses on the thickness and optical axis orientation

Since the two determining parameters for phase shift correction are crystal thickness and orientation of the crystal's optical axis, it is of paramount importance to study their acceptable tolerances to ensure that the correct phase shift

is induced. It is therefore necessary to determine precisely the acceptable variations in crystal thickness and optical axis orientation to guaranty compliance with the required PER performances. For this purpose, the crystal thickness is varied by different orders of magnitude, and the orientation of the optical axis is varied too.

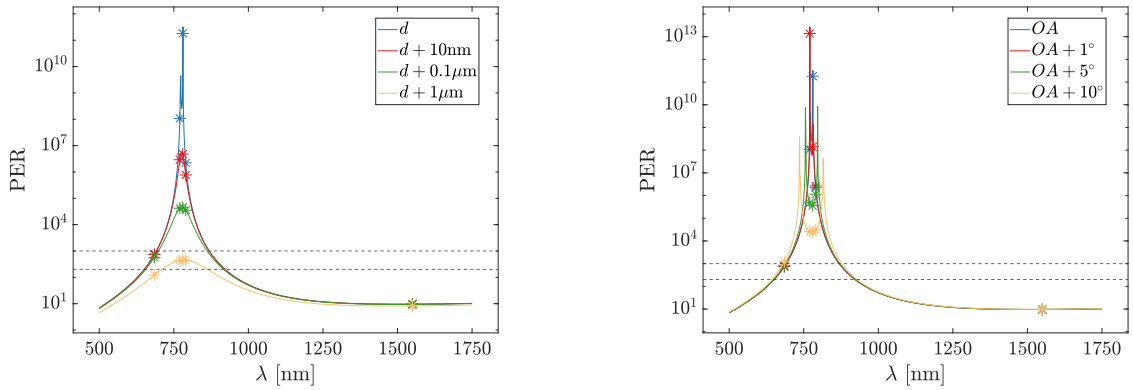

(a) Thickness.

(b) Optical axis orientation.

Figure 5.10 – **Tolerance analyses on the thickness and orientation of the optical axis of the MgF_2 crystal**. Initial thickness d is for QKD optimization.

The parameter with the greatest impact is the crystal thickness, and it follows from Figure 5.10a that a tolerance of 0.1 μm is acceptable. This tolerance is in line with the order of magnitude of the tolerance that waveplate manufacturers are able to provide (Edmund Optics, 2024). The impact of the orientation of the optical axis on the order of magnitude of the PER is much less. Tolerances of the order of several degrees are acceptable, but still lead to a progressive decrease in order of magnitude, to the benefit of other wavelengths, which is not the case for the thickness tolerance.

Considering these errors simultaneously gives the results shown in Figure 5.11. However, it is important to note that taking both tolerances simultaneously into account can have a positive or negative impact, depending on whether the combination of thickness and optical axis orientation results in a final phase shift that is closer or less close to the desired phase shift. Consequently, as a safety measure, and given that the alignment of the optical axis can be achieved without too much difficulty with a smaller tolerance, the tolerance on the alignment of the optical axis is reduced to the order of a degree.

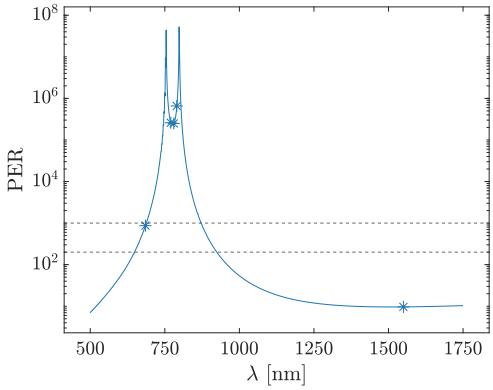

(a) $d + 0.1$ μm, $OA + 10°$.

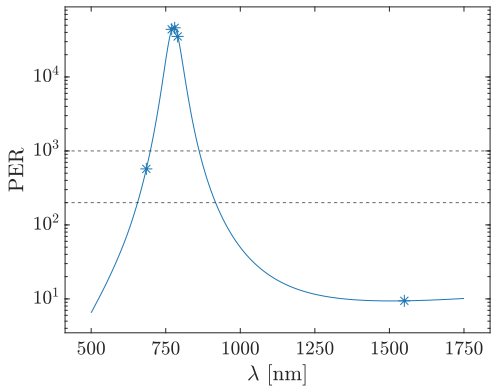

(b) $d + 0.1$ μm, $OA + 1°$.

Figure 5.11 – **PER results for simultaneous consideration of thickness and optical axis alignment errors.**

5.4.2 Optimization using two crystals

The previous study has hinted at a way to optimize the performances in terms of PER at multiple wavelengths simultaneously. However, as the adage goes, there is no free lunch. Achieving the objectives using the principle of birefringence requires the use of multiple crystals, and to rigorously determine both their thicknesses and orientations. For simplicity of assembly and to minimize alignment and thickness errors, the feasibility of using two crystals is being investigated firstly.

Equation 5.11 is modified as below[3] for light propagation through two crystals of thicknesses d_1 and d_2, and birefringences Δn_1 and Δn_2.:

$$\Delta\varphi(\lambda) = \frac{2\pi}{\lambda} d_1 \Delta n_1(\lambda) + \frac{2\pi}{\lambda} d_2 \Delta n_2(\lambda). \tag{5.20}$$

The choice of crystals is no longer as free as before. While they still need to be transparent at the wavelengths of interest, and remain financially affordable and manufacturable with sufficient ease, the two crystals must also exhibit different birefringences in function of the wavelength (Miller et al., 2022). If two crystals with a very similar birefringence were used, due to the almost identical nature of the crystals, any adjustment made one the thickness of one crystal to optimize a different wavelength would also affect the other optimized wavelength. Thus, changing the thickness of one to optimize for one wavelength would negatively impact the PER at other wavelengths due to the significant difference between the phase shifts to be corrected. However, if the crystals exhibit sufficiently different birefringences, this negative impact can be compensated by the difference in birefringence. This is also the reason why two identical crystals can't be used to optimize the PER at two wavelengths of significantly different retardance.

The second selected crystal that meets these criteria is aluminum oxide (Al_2O_3). The difference between the birefringences of the two crystals is visible in Figure 5.12.

[3]The sign before each term could be different, depending on the orientation of the corresponding crystal. In general, this expression remains valid as the sign can be absorbed into the thickness of the crystal, which can be either negative or positive, as explained earlier.

With the choice of crystals made, Equation 5.20 still has two variable parameters, d_1 and d_2. Therefore, several combinations of thicknesses can optimize one wavelength. This degree of freedom can be effectively utilized for optimization at two wavelengths, by establishing a system of two equations with two unknowns, whose exact solution provides the necessary thicknesses for the two crystals:

$$\begin{cases} -\delta(\lambda_1) = \dfrac{2\pi}{\lambda_1}\Big(d_1\Delta n_1(\lambda_1) + d_2\Delta n_2(\lambda_1)\Big), \\ -\delta(\lambda_2) = \dfrac{2\pi}{\lambda_2}\Big(d_1\Delta n_1(\lambda_2) + d_2\Delta n_2(\lambda_2)\Big). \end{cases} \tag{5.21}$$

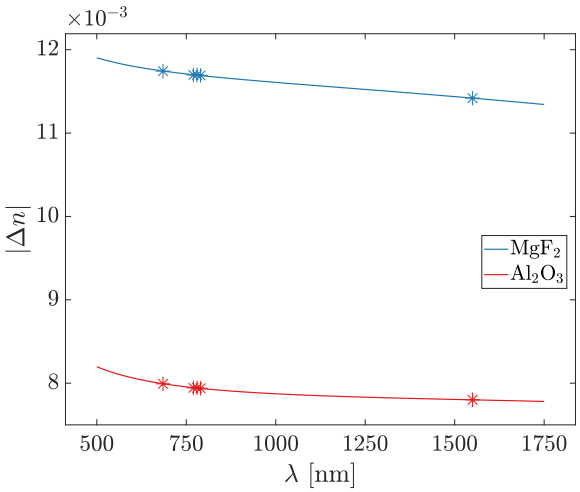

Figure 5.12 – **Birefringent properties of MgF_2 and Al_2O_3.**

Solving the system for optimization in the three possible configurations (beacon-QKD, telecommunication-QKD and beacon-telecommunication) yields the results of Figure 5.13, with the associated thicknesses d_1 for MgF_2, and d_2 for Al_2O_3.

Table 5.3 – **Required thicknesses for the crystals in function of the wavelengths to optimize.** *OA* denotes the orientation of the optical axes of the crystals.

λ	d_1	d_2	OA_1	OA_2
Beacon-QKD	0.301 mm	0.440 mm	z	z
Telecommunication-QKD	2.345 mm	3.450 mm	z	z
Beacon-Telecommunication	3.674 mm	5.396 mm	z	z

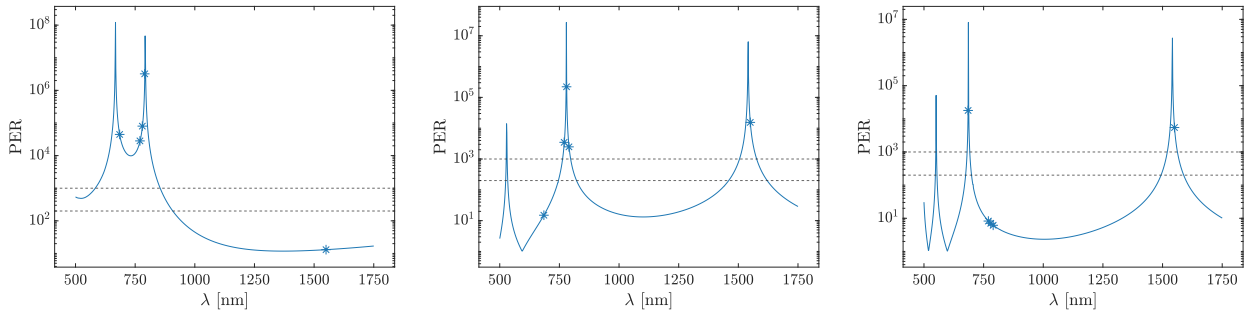

(a) Beacon-QKD. (b) Telecommunication-QKD. (c) Telecommunication-beacon.

Figure 5.13 – **PER in function of wavelength for the possible optimization configurations.**

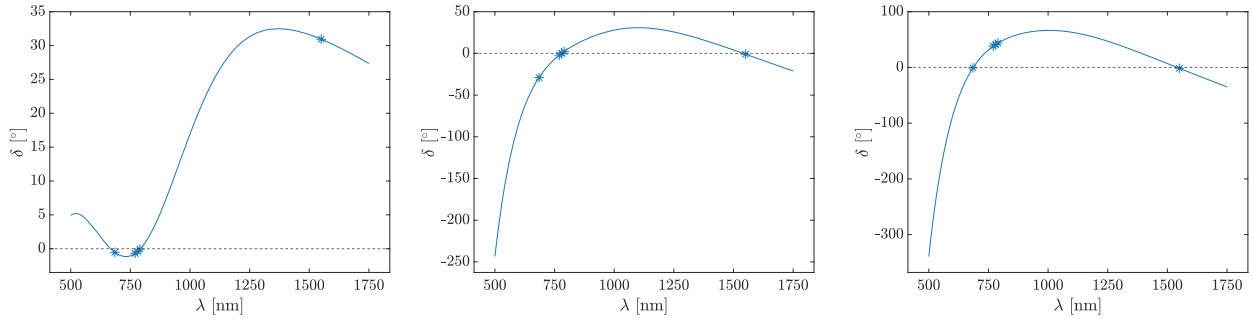

(a) Beacon-QKD. (b) Telecommunication-QKD. (c) Telecommunication-beacon.

Figure 5.14 – **Phase shift in function of wavelength for the possible optimization configurations**.

As for the study of high-order solutions, large wavelengths have a low crystal-induced phase shift derivative, and so larger optimized wavelength bands. Moreover, the appearance of parasite optimized wavelength bands must be confirmed by analyzing the corresponding phase shift to confirm optimization and not a polarization orientation reversal. It turns out that for the considered range of wavelengths, all the parasite peaks correspond to a reversal of the polarization orientation.

Figure 5.13 illustrates the impossibility for the two-wavelengths optimization to meet the requirements for the PER at the three wavelengths simultaneously, due to the wavelength band being too narrow to cover the beacon and QKD wavelengths simultaneously when optimizing for telecommunication, or the absence of a peak at the telecommunication wavelength in the case of optimization at both QKD and beacon wavelengths. These results suggest that the addition of a third crystal is the preferred solution for simultaneously optimizing three wavelengths.

5.4.3 Optimization using three crystals

As with two crystals, the determination of the thickness of each crystal is based on knowledge of the phase shifts and birefringence properties of the crystals. Thus, the thicknesses d_1, d_2 and d_3 of the zero-order solution are naturally derived from

$$\begin{cases} -\delta(\lambda_1) = \dfrac{2\pi}{\lambda_1}\Big(d_1\Delta n_1(\lambda_1) + d_2\Delta n_2(\lambda_1) + d_3\Delta n_3(\lambda_1)\Big), \\ -\delta(\lambda_2) = \dfrac{2\pi}{\lambda_2}\Big(d_1\Delta n_1(\lambda_2) + d_2\Delta n_2(\lambda_2) + d_3\Delta n_3(\lambda_2)\Big), \\ -\delta(\lambda_3) = \dfrac{2\pi}{\lambda_3}\Big(d_1\Delta n_1(\lambda_3) + d_2\Delta n_2(\lambda_3) + d_3\Delta n_3(\lambda_3)\Big). \end{cases} \tag{5.22}$$

The third crystal, selected using the same criteria as the first two, is zinc oxide (ZnO). For comparison, its birefringence properties are given in Figure 5.15. By solving the system of equations, the thicknesses and orientations of the optical axes are found, and are provided in Table 5.4.

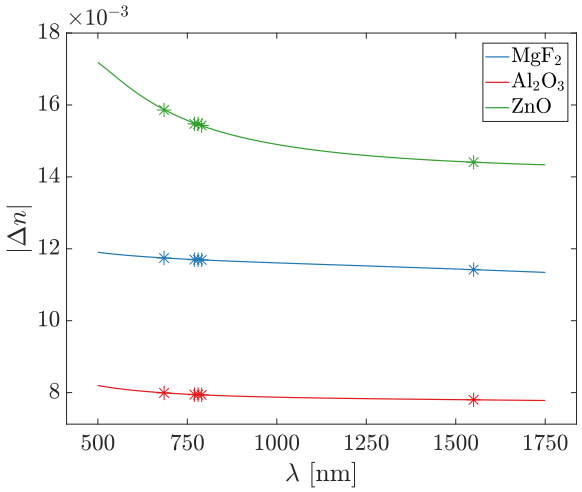

Figure 5.15 – **Birefringent properties of MgF_2, Al_2O_3 and ZnO.**

Table 5.4 – **Required thicknesses for the crystals for simultaneous optimization of all desired wavelengths.** *OA* denotes the orientation of the optical axes of the crystals.

λ	d_1	d_2	d_3	OA_1	OA_2	OA_3
Beacon-QKD-Telecommunication	1.308 mm	2.092 mm	0.087 mm	z	z	z

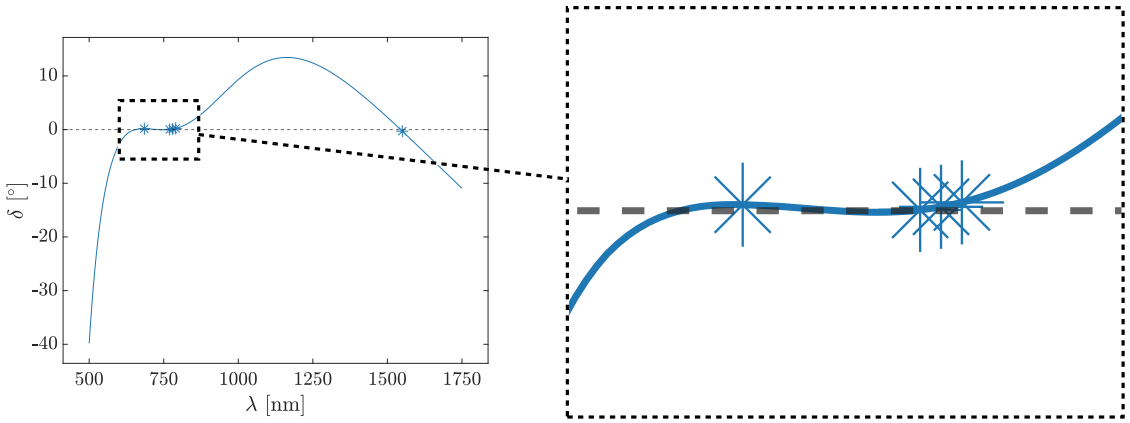

(a) Phase shift over a broad spectrum of wavelengths.

(b) Zoom on the QKD band and beacon wavelength, revealing an additional wavelength with zero phase shift.

Figure 5.16 – **Phase shift in function of wavelength for simultaneous optimization of all wavelengths**.

Exact compensation of the retardance at the wavelengths of interest using three crystals provides a feasible solution. Performance is on target over a wide band covering the first two wavelengths, and there is also a significant margin over the third wavelength thanks to its wide bandwidth. Given the small thickness of the ZnO crystal, as explained above, this solution involves using a fourth crystal of perpendicular optical axis and of random thickness, so that the thickness of the third crystal is modified such that the difference in thickness between the two is the thickness calculated theoretically for the third crystal. The PER at the relevant wavelengths for this project are given in Table 5.5. Eventually, one should keep in mind that all the results presented for the PER are for ±45° polarization, which is

the worst-case scenario. For all other types of linear polarization, the PER is higher.

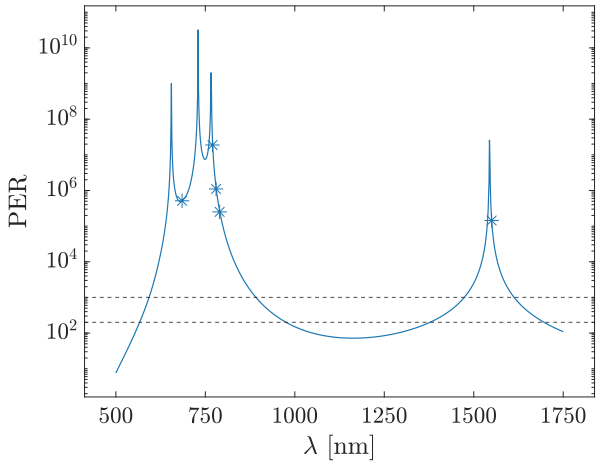

Figure 5.17 – **PER in function of the wavelength for simultaneous optimization of all desired wavelengths**. All objectives are reached. Unwanted optimization between 685 nm and 770 nm comes from an additional point with zero phase shift in this region.

Table 5.5 – **PER obtained using the three crystals optimization.**

Wavelength	**Telescope PER**	**Targeted PER**
685 nm	514 574 : 1	200 : 1
770 nm	1 8881 400 : 1	1000 : 1
780 nm	103 480 : 1	1000 : 1
790 nm	251 043 : 1	1000 : 1
1550 nm	143 952 : 1	200 : 1

5.4.4 Merit function optimization

Previously, the method for determining crystal thickness and orientation was based on the exact resolution of the phase shift equations. This has the advantage of compensating the phase shifts exactly, but sometimes at the cost of a narrow optimized wavelength band. Alignment errors or excessively tight thickness tolerances could significantly degrade the performances to the extent of non-compliance with the objectives. To avoid this, an alternative approach to the problem involves optimizing (minimizing) a *merit function* over a broader range of wavelengths. The expression of this function relies on the phase shifts, since they provide an immediate measure of performance. As the optimized wavelength band using three crystals is large around the areas of interest, the merit function optimization is applied using two crystals for the search of an equivalent solution only using two crystals:

$$M_{j,k} = \sum_{i=1}^{l} \left(\frac{\Delta\varphi_{i,j,k} - \delta_i}{\delta_i} \right)^2 \cdot \omega_i \tag{5.23}$$

$\Delta\varphi_{i,j,k}$ is the calculated phase shift for thicknesses d_j and d_k corresponding to the first and second crystal, respectively, for each wavelength i to be optimized. δ_i is the phase shift to induce at wavelength i for optimization. The number of wavelengths to optimize is denoted l. Normalization ensures that no term in the sum dominates the others. A *weight function* ω is applied to regulate the importance of each individual wavelength.

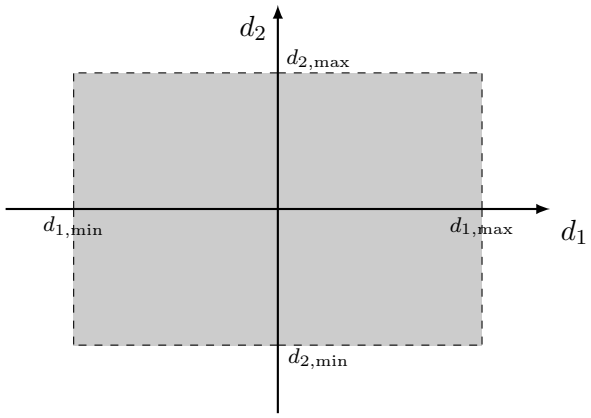

Figure 5.18 – **Spatial domain.** Maximum values for the thicknesses are free of choice.

One possible way to optimize the merit function is through large-scale testing, by testing all possible combinations of thicknesses within a given range. The spatial discretization of the domain involves a large number of thickness combinations to test, and this highly refined discretization may require a significant amount of memory for calculations, which can be problematic to avoid overlooking a solution. For these reasons, large-scale testing is not considered[4], and the optical axis angle and thickness for each crystal are determined using the non-linear multivariable solver `fmincon`, by minimization of M (Miller et al., 2022).

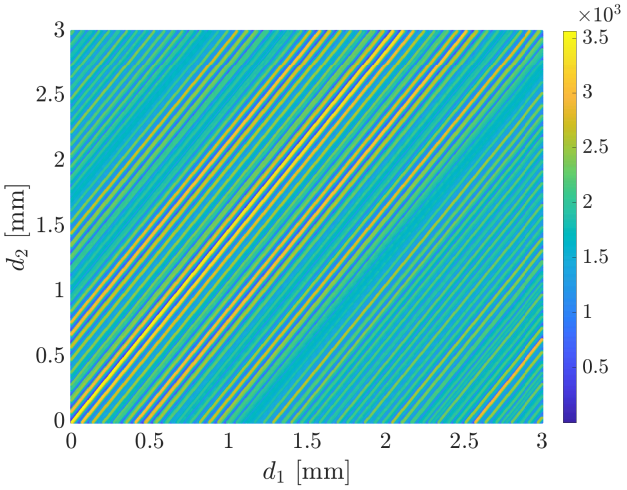

Figure 5.19 – **General shape of the merit function**. The diagonals of equal merit function value reflect the link between the phase shift induced by the crystals and their thicknesses. Since the induced phase variation is periodic, moving along the diagonals means exploring higher-order solutions. Spatial domain representation has been restricted for the ease of visualization.

Given the strong dependence of non-linear numerical solvers on initial conditions, the search for optimum thicknesses is carried out by testing all possible initial conditions in the search domain, with a spatial step derived from Figure 5.19 to ensure all areas are explored. The domain extends from a null thickness to 10 mm thickness for each crystal, in order to encompass the thicknesses of the exact solutions for each optimization case, while leaving considerable scope for exploring further thicknesses corresponding to higher orders.

[4]With the exception of Figures 5.19 and 5.21, where this method is used to obtain a visual representation of the merit function.

In an attempt to achieve the objectives using two crystals, it is chosen to optimize weight functions $\omega_1, \omega_2, \omega_3$ and ω_4. Weight function ω_5 aims to compare the exact resolution of the phase shift equations to the optimization of the merit function.

- ω_1: unitary weight function for the three main wavelengths.
- ω_2: weight function corresponding to the imposed priority order.
- ω_3: weight function attempting to achieve good performances at beacon and QKD wavelengths, corresponding to the priority order, by fixing their weights considerably higher than the telecommunication wavelength.
- ω_4: unitary weight function considering the extremities of the QKD band, using two crystals.
- ω_5: weight function with priority order considering the extremities of the QKD band, using three crystals.

Table 5.6 – **Weight functions**.

	Beacon	QKD −10 nm	QKD	QKD +10 nm	Telecommunication
ω_1	1	0	1	0	1
ω_2	2	0	3	0	1
ω_3	5	0	10	0	1
ω_4	1	1	1	1	1
ω_5	2	3	3	3	1

The thicknesses and orientations of the optical axes of the crystals, determined by optimizing M using the `fmincon` solver for the different weight functions ω, are provided in Table 5.7.

Table 5.7 – **Optimization results for the different weight function**.

	d_1	d_2	d_3	OA_1	OA_2	OA_3
ω_1	7.321 mm	7.579 mm	/	x	z	/
ω_2	7.321 mm	7.579 mm	/	x	z	/
ω_3	5.347 mm	1.685 mm	/	z	z	/
ω_4	0.418 mm	0.612 mm	/	z	z	/
ω_5	1.397 mm	2.239 mm	0.096 mm	z	z	z

Figure 5.20 confirms the difficulty of optimizing the QKD and beacon wavelength bands, along with the telecommunication wavelength. This stems from the significant phase shift difference between the two bands. The optimization naturally converges to unsuitable very high order solutions. Applying a priority order for optimization of the three relevant wavelengths is also not enough. One has to optimize the full QKD wavelength band for better results, at the expense of bad PER for the telecommunication. Eventually, the merit function optimization using three crystals is applied for the sake of completeness. Results are matching the objectives, and are as satisfactory as the results of the exact solution.

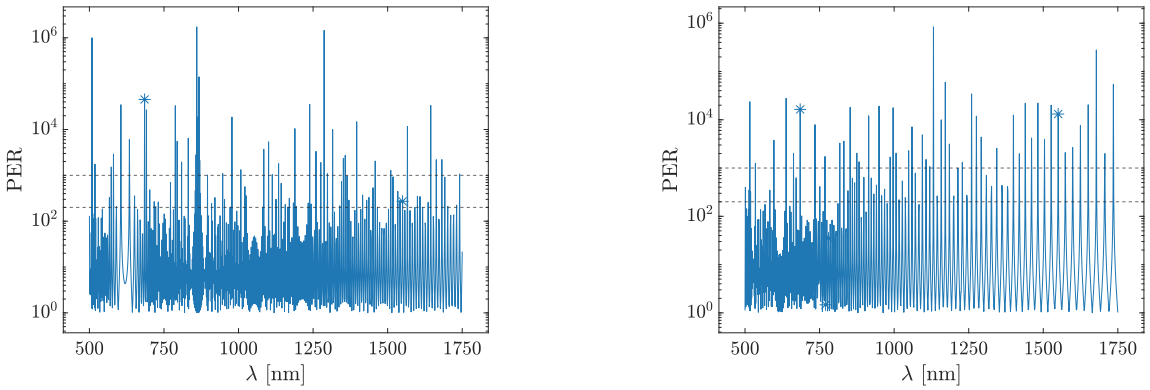

(a) ω_1, ω_2.

(b) ω_3.

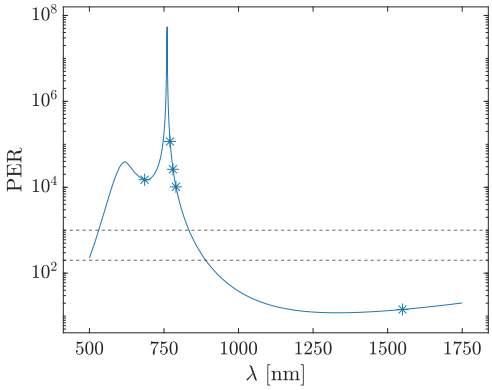

(c) ω_4.

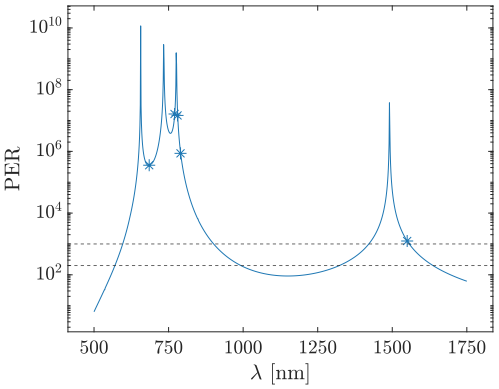

(d) ω_5.

Figure 5.20 – **PER in function of wavelength for the different weight functions**. Objectives are not reached using two crystals. The merit function optimization confirms the impossibility of using two crystals to optimize all wavelength bands.

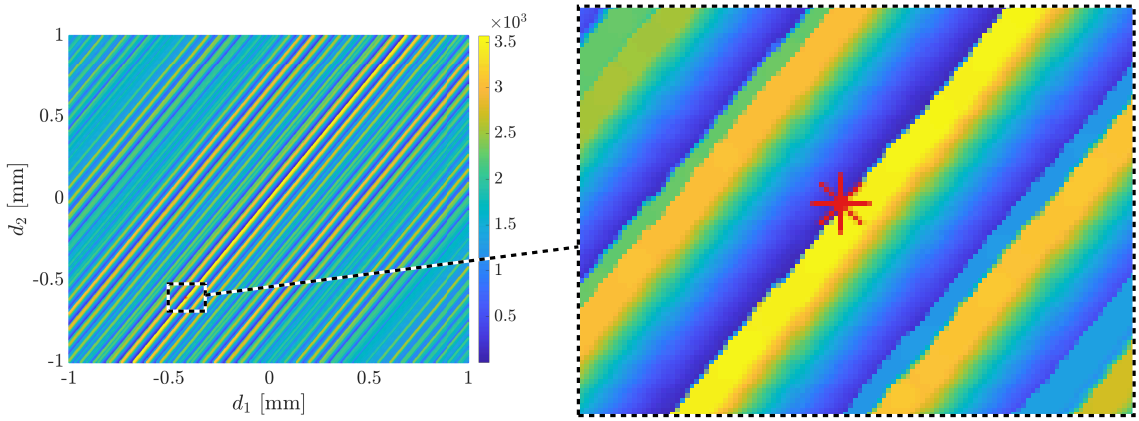

(a) Spatial domain.

(b) Zoom on the location of the solution corresponding to ω_4. The red dot indicates the position of the optimal solution in the domain.

Figure 5.21 – **Merit function corresponding to ω_4.** Spatial domain representation has been restricted for better visualization.

Part V

Experimental measurements

Chapter 6

Experimental study of polarization characteristics

The first task of this project was to determine the retardance caused by the reflections on the various mirrors, particularly induced by the third mirror M_3. The previous chapters demonstrated the methodology for characterizing and correcting it. However, the retardance is determined from the telescope model as designed in the *Ansys Zemax OpticStudio* software. This model is based on standard models for the coatings on the various mirrors, and the telescope model is thus naturally subject to modeling errors.

Since retardance is the basis of the problem in this project, it is of paramount importance that it corresponds to the retardance induced by real mirrors that will be used for MOCA. To this end, the retardance induced by a mirror sample is studied by the discipline of *ellipsometry*. The variation of the azimuth angle is also studied for completeness.

6.1 Ellipsometry

As a consequence of Fresnel's equations, polarized light at non-normal incidence on an optical surface will undergo a phase shift between its components of polarization. This change of polarization is dependent on the AOI, and on the material properties of the optical surface. Ellipsometry is the practical discipline studying the change of polarization, by determination of the retardance[1] and azimuth angle, Δ and ψ respectively (called the ellipsometric parameters) after reflection on the optical surface, from intensity measurements at the detector.

The experimental setup for ellipsometry consists of two parts. The first branch, called the *polarization state generator*, consists of a light source accompanied by polarizing elements such as polarizers or retarders. After reflection on the optical surface, light arrives in the second branch, called the *polarization state detector*, which generally contains an analyzer (polarizer), followed by a detector to measure the intensity (Tompkins and Irene, 2005).

Ellipsometry consists of four key stages aimed at determining the ellipsometric angles ψ and Δ:

1. Generation of a polarized light beam.
2. Reflection on an optical surface leading to a new polarization state.

[1] The retardance, denoted δ in the previous chapters, is written Δ for consistency with the literature.

3. Analysis of the new polarization state.

4. Determination of the ellipsometric angles.

Step 1 and 3 happen in the polarization state generator and polarization state detector, respectively.

6.1.1 Types of ellipsometers

The first types of ellipsometers to be developed were *nulling ellipsometers*. These are made up of the components listed above, and the ellipsometric angles are determined by adjusting the optical parameters, such as the polarizer angles, of the components until a null signal is obtained at the detector (Azzam and Bashara, 1987).

Because the nulling ellipsometer is slow in its process, and because of the dark current with its associated noise inevitably present in detectors, the *photometric ellipsometer* was developed. In this type of ellipsometers, two configurations are possible. The first one varies the angle of the polarizer in the polarization state generator branch, while keeping the angle of the analyzer fixed. The second, and more common option, is to reverse the roles, i.e. vary the angle of the analyzer while keeping the angle of the polarizer constant. These two configurations are respectively called the *rotating polarizer ellipsometer* (RPE) and *rotating analyzer ellipsometer* (RAE). As a consequence of the angle variation, the intensity measurements at the detector vary sinusoidally. It is then possible, from a spectral decomposition of the signal using Fourier's theory, to deduce the ellipsometric parameters (Motschmann and Teppner, 2001; Gonçalves and Irene, 2002).

Depending on the application, ellipsometry can be spectroscopic, and therefore requires monochromators in the setup to study each wavelength separately. Furthermore, it has been shown by Aspnes (1974) that the uncertainty on the retardance using photometric ellipsometry is greatest when light is linearly polarized. To overcome this problem, a compensator is introduced into the polarization state generator arm to induce ellipticity, which does not change the retardance induced by reflection, as it is independent of the type of polarization. Moreover, this type of ellipsometer is the best possible choice when investigating broad spectral bands, having the added advantage of being able to operate at low light intensity (Tompkins and Irene, 2005; Gonçalves and Irene, 2002).

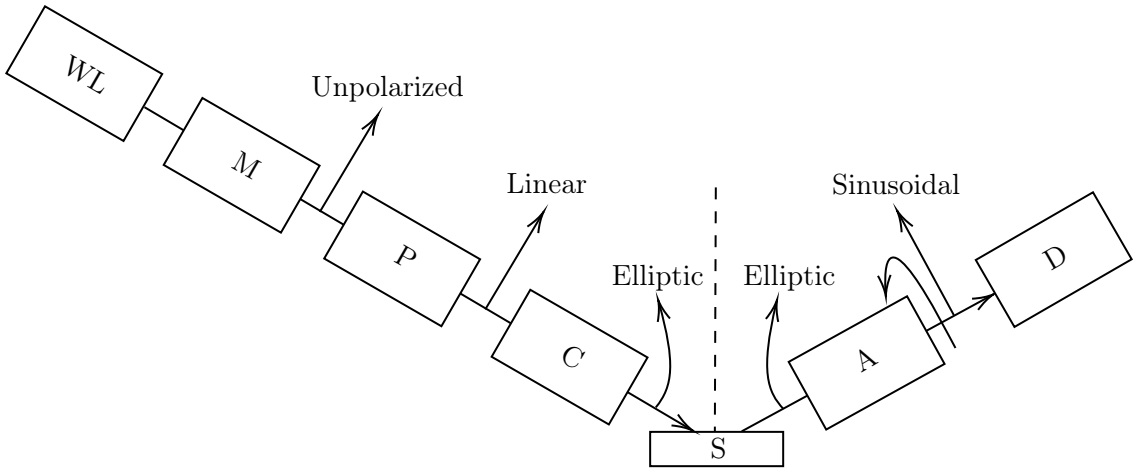

Figure 6.1 – **Rotating analyzer ellipsometer**. WL, M, P, C, S, A, and D stand for White Light, Monochromator, Polarizer, Compensator, Sample, Analyzer and Detector, respectively. The compensator is placed to induce ellipticity. *Adapted from Tompkins and Irene (2005).*

6.1.2 Determination of the ellipsometric parameters from polarization formalisms

Since current detectors only measure intensities, the ellipsometric parameters ψ and Δ must be deduced from this signal. In the presence of fully polarized light, it is possible to use the Jones formalism to describe each component of the ellipsometer by its Jones matrix, in order to deduce the equivalent Jones matrix as described in Chapter 2 by successive multiplications of the component matrices. However, in order to take into account the non-ideality of depolarizing components, and for generality, the Stokes formalism is used for a brief description of the ellipsometer. The case of the RAE is studied for illustration. As with the Jones formalism, the Mueller matrices of the components are successively multiplied:

$$I_{\text{th}}\,\mathbf{s}_D = \mathfrak{R}\left(-A'\right)\mathbf{M}_A\mathfrak{R}\left(A'\right)\mathbf{M}_S\mathbf{M}'\mathfrak{R}\left(-P'\right)\mathbf{M}_P\mathfrak{R}\left(P'\right)\left(I_S\mathbf{s}_S\right). \tag{6.1}$$

The normalized Stokes vector at the detector is written $\mathbf{s}_D$, and I_{th} and I_S are the irradiance at the detector and the source, respectively. The matrices $\mathbf{M}_A$ and $\mathbf{M}_P$ denote the Mueller matrices of the analyzer and polarizer, respectively, and $\mathbf{M}_S$ is the sample's Mueller matrix. Matrix $\mathfrak{R}$ is a rotational transformation that converts the Stokes vector or Mueller matrix from the global coordinate system to the local coordinate system of the element. Eventually, matrix $\mathbf{M}'$ is the Mueller matrix of the compensator in the global reference frame. The ellipsometric parameters are deduced from a Fourier analysis of the intensity at the detector, by varying the analyzer angle.

6.2 Experimental measurements

6.2.1 Mirror sample

The sample provided by AMOS for the ellipsometric measurements is a flat aluminium mirror sample coated with protected silver. It has previously been used for the qualification of mirror coatings for the CHIME (Copernicus Hyperspectral Imaging Mission for the Environment) spectrometer system instrument. In total, the coating consists of 8 layers of different materials: chromium (Cr), nichrome (NiCr), silicon dioxide (SiO_2), tantalum (Ta), tantalum oxide (Ta_2O_5), hafnium oxide (HfO_2), Al_2O_3 and silver (Ag). Due to the confidentiality imposed by the manufacturer of the coating, CILAS, the exact thickness of each layer is unknown. The total thickness of the coating, however, is known and is about 200 nm.

Figure 6.2 – **Mirror sample**.

6.2.2 Ellipsometer

To measure the ellipsometric parameters, experimental measurements were carried out at Centre Spatial de Liège (CSL), which is equipped with the *SENresearch 4.0* spectroscopic ellipsometer. It covers a wide spectral range from the deep ultraviolet ($\lambda = 190$ nm) to the shortwave infrared ($\lambda = 3500$ nm), with high SNR and selectable spectral resolution. Thanks to the step scan analyzer (SSA), which is

a unique feature of the SENresearch 4.0 spectroscopic ellipsometer, there are no moving optical parts during data acquisition, guaranteeing optimum measurement results. The accuracy on the ellipsometric parameters are given in Table 6.1 (SENTECH Instruments, 2024).

Table 6.1 – **Accuracy of the ellipsometer**.

Ellipsometric parameter	**Accuracy**
Δ	0.06°
ψ	0.03°

Spectralray/4 is the software used to configure the ellipsometer and perform measurements. It is used in interactive mode through a graphical interface to perform the required ellipsometric measurements for this work. For the sake of comparison and to illustrate the importance of the M_3 mirror, a spectral range from 500 nm to 1750 nm, and incidence angles from 42° to 48°, have been considered.

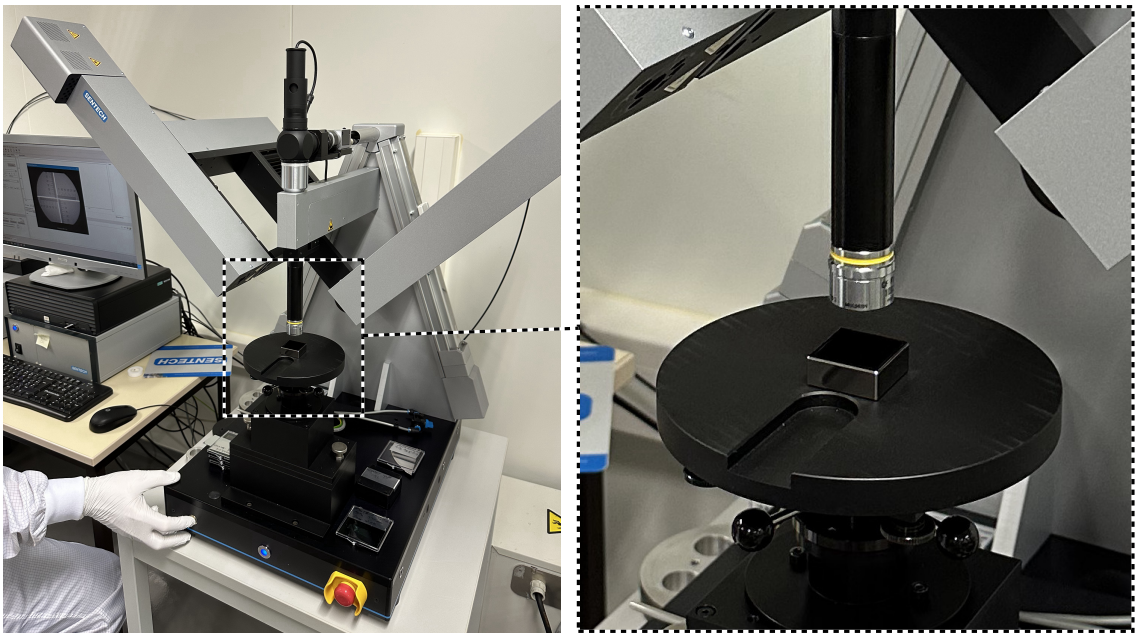

(a) SENresearch 4.0 spectroscopic ellipsometer. (b) Mirror sample in place for measurements.

Figure 6.3 – **Experimental setup at CSL**.

6.2.3 Measurement of the retardance

Measuring retardance is fundamental to the success of the MOCA project. To this end, the study of retardance based on the standard model of the protected silver coating in *Ansys Zemax OpticStudio*, carried out previously Chapter 4, is compared with the experimental measurements provided by the ellipsometer. The difference between the results in Figure 6.4a directly leads to the conclusion that the standard model, composed solely of SiO_2, Al_2O_3 and Ag, does not perfectly fit the measured coating. However, by proceeding inversely through the modification of the composition and thicknesses of the layers of the modeled coating, it is possible to reconcile the results in the considered wavelength band. The results of this procedure are illustrated by the *reverse-engineered model* curve, providing a good qualitative approximation of the experimental measurements. Deviations are on the order of a few degrees.

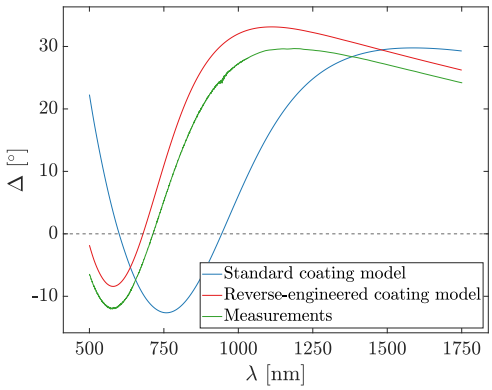

(a) Comparison of the retardance from experimental measurements to the *Ansys Zemax OpticStudio* models.

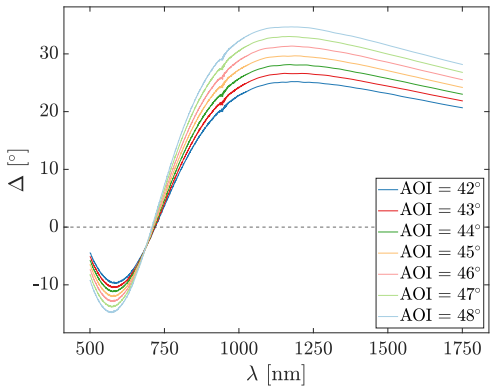

(b) Evolution of the retardance with varying AOI.

Figure 6.4 – **Retardance.**

It is important to be aware that even if the coating characteristics of the sample were perfectly known, a coating model with the same characteristics would still yield different results. The discrepancies would then arise from differences in optical parameters of the layers. For instance, the coating deposition method has an impact on the optical parameters of the coating. Depositing a substrate layer by ion beam sputtering or by magnetron sputtering would thus result in different optical properties for the coating layers. In addition, other parameters such as deposition rate or temperature influence optical properties. Indeed, variations in deposition techniques and parameters affect the energy with which atoms and molecules arrive on the substrate, leading to different atomic arrangements, and consequently, slight differences in optical properties.

Moreover, it should be noted that the ellipsometer itself is not perfect (see Table 6.1), and offers only a certain degree of precision in measurements.

Since the AOI on M_3 varies across the pupil and is not exactly 45°, the behavior of an incident photon deviates from what would occur if the AOI was precisely 45°. Thus, a potential additional explanation for the deviation from measurements would come from a slight difference in AOI, which would be consistent with the observations in Figure 6.4b.

In conclusion, although the exact characteristics of the sample are unknown, and as the behavior of the retardance curve is the same for both models, it confirms the correct implementation of the Jones formalism, and the correct characterization of the telescope retardance. It is worth remembering, however, that since every model is an approximation, and given the dependence of optical properties e.g., on the various parameters listed above, it is not possible to obtain exactly the same results, and experimental measurements will always be the results on which to base the characterization of the retardance of a mirror.

6.2.4 Measurement of the azimuth angle

Although SpeQtral has not imposed any constraint on this parameter, the azimuth angle plays an important role for algorithms such as BB84 in discerning the polarization state, and must consequently be maintained. As with the retardance, a deviation between the standard coating model and the exper-

imental measurements is observed in Figure 6.5a, once again highlighting the differences between the coatings. The reverse-engineered model shows, as expected, great consistency with the measurements and closely matching values, with a maximum deviation about a tenth of a degree.

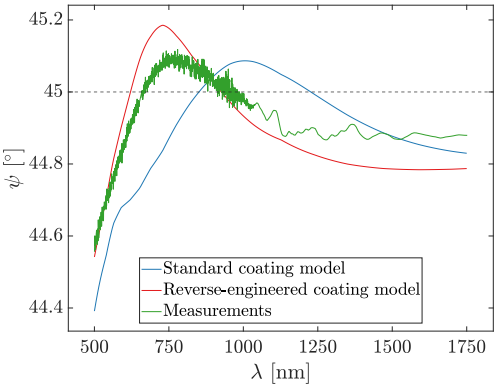

(a) Comparison of the polarization orientation from experimental measurements to the *Ansys Zemax OpticStudio* models.

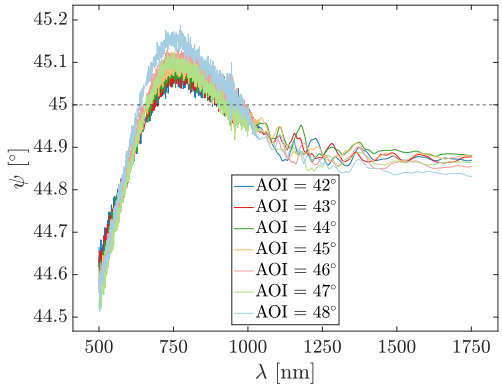

(b) Evolution of the polarization orientation with varying AOI.

Figure 6.5 – **Polarization orientation.** Initial state of polarization is 45°. The difference in flatness in the measurements results from a non-constant step size used on the wavelength by the ellipsometer.

Additionally, the magnitude of the variations on ψ remains on the order of a few tenths of a degree, allowing the different states to be distinguished from one another. The impact of the AOI shown in Figure 6.5b is of the order of a tenth of a degree.

All the elements provided in the discussion of the retardance to explain the differences between the results of the models and the experimental results remain obviously applicable. The conclusion is also the same: experimental results will always be the ones to rely on, and models can only provide approximations for a qualitative characterization of the results.

6.3 Telescope characterization procedure and conclusion

As demonstrated and discussed in this chapter, relying on models is not sufficient, and experimental measurements are required to characterize ellipsometric parameters quantitatively. Since ellipsometry provides the necessary experimental measurements with a high degree of accuracy, AMOS can use it to characterize the M_3 mirror. Consequently, the telescope can be accurately assessed for its polarization characteristics.

Chapter 5 studied the feasibility of using crystals to correct the retardance, and specified the tolerance that needs to be met on the thickness and optical axis orientation of the crystals. In practice, however, the objective remains the induction of the correct retardance value at the required wavelengths. This therefore means that the required optical path length must be reached, by progressive manufacturing of the crystals, ensuring that any tolerance related to the thickness, the optical axis orientation, or to the dispersion of the crystals, is inherently addressed through the achievement of the desired retardance. This methodology thus guarantees accurate results for the characterization, and rigorous crystal manufacturing will then enable retardance correction and thus the attainment of the targeted PER.

Part VI

Conclusion

Chapter 7

Conclusion and perspectives

7.1 Thesis summary

With the aim of studying changes in polarized light through MOCA, this report firstly introduces electromagnetic waves and their possible polarization, along with a discussion of the different types of polarization and a useful introduction to the associated mathematical formalism. The principles of QKD, including the theory required to understand it, follows and demonstrates the high security of this method, illustrated using the BB84 algorithm. The MOCA project, which aims to develop and demonstrate international use cases for QKD, is discussed with particular emphasis on the optical design and information useful for this work. The importance of the project is considerable both for AMOS and for the world of secure communications in the years to come.

The work carried out usefully focuses on the characterization of the telescope based on the adapted Jones formalism for fully polarized light. The promising results of this study show the feasibility of characterizing optical communication antennas using the Jones formalism through a general methodology as studied in Chapter 4. Thanks to this methodology, the phase shift between the orthogonal components of polarization, mainly responsible for poor performance in terms of PER, can be derived for each desired wavelength, and in particular for each wavelength useful to the project. It is shown that the retardance is too large to reach the targeted PER values, with values on the order of several degrees or even tens of degrees compared to the desired null phase shift, representing the case of maximum PER.

Poor performance in terms of PER is unacceptable for the MOCA project, and in general for QKD based on the polarization of light. To overcome this problem, a detailed study implementing the use of birefringent crystals is being carried out, with the aim of studying the feasibility of correcting the phase shift between the orthogonal components of polarization. The approach shows that this correction is feasible for wavelength bands that are free of choice, but for which the thicknesses of the crystals used and the orientation of their optical axes are rigorously determined. Crystals of different birefringence are, however, needed to achieve good performance in terms of PER for significantly different wavelength bands, if the phase shift induced by the telescope is significantly different. In order to optimize the three wavelength bands used for the MOCA project, the use of three crystals is necessary.

Eventually, the ellipsometric measurements carried out at the CSL enabled to conclude that the Jones formalism had been correctly implemented, and demonstrated the need for experimental measurements to characterize a manufactured mirror.

The key conclusions of this study are that it is possible to characterize optical telecommunication antennas by polarization formalisms such as that of Jones, and that the latter allow considering ways to maintain polarization through the telescope. Using correction methods such as birefringence, the polarization state can be maintained, and QKD algorithms exploited.

7.2 Perspectives

The study concluded that it was necessary to use the same number of crystals as the number of wavelengths to optimize. However, using merit function optimization with different crystals, it could theoretically be shown that optimizing at all wavelengths with fewer crystals might be possible, if the crystals present a highly variable dispersion curve. This would be a stroke of luck, and in practice, taking the risk of using fewer crystals than the number of wavelengths to optimize is not advisable because it is unlikely to achieve the same success again. It is thus better to play it safe by using the same number of crystals as wavelengths, as this method has proved its worth.

Although this is not the case at present, constraints on variations in polarization orientation could be imposed by SpeQtral in the future. A closer look at this parameter would then need to be taken to guide the search for crystals, and potentially the coating if desired, to limit variations.

Moreover, during this work, research focused on a way of maintaining polarization through the use of birefringent crystals. However, this is not the only way, and others should be investigated. One example is the study of mirror coatings, a method that has already been proposed in the literature as discussed in Section 5.1. In addition, Chapter 6 demonstrated the possibility of adjusting the modeled delay curve by modifying the thickness and composition of the coating layers. Consequently, the coatings of the M_3 mirror could be changed and a study conducted on a choice of coating maintaining polarization at wavelengths useful to the project. Thus, a detailed study of the coatings should be carried out to gain an in-depth understanding of the behavior of the retardation curve, with the aim of achieving zero retardance at the targeted wavelengths. Optimizing a coating for one or more wavelengths relevant to the MOCA project could then potentially reduce the required number of crystals.

Eventually, AMOS plans to use liquid crystals to correct the phase delays caused by the corrector mirrors. This solution could also be used to correct the retardance of M_3, and potentially also in combination with an optimized coating.

Part VII

Appendices

Appendix A

Electromagnetic waves

A.1 Wave equation for the magnetic field

The determination of the wave equation for the magnetic field can be carried out in a similar manner to the derivation of that for the electric field. By taking the curl of Equation 2.4, one has

$$\overrightarrow{\nabla} \times \left(\overrightarrow{\nabla} \times \overrightarrow{H} \right) = \overrightarrow{\nabla} \times \left(\overrightarrow{J} + \frac{\partial \overrightarrow{D}}{\partial t} \right). \tag{A.1}$$

and making use of the vectorial calculus relation

$$\overrightarrow{\nabla} \times \left(\overrightarrow{\nabla} \times \overrightarrow{H} \right) = \overrightarrow{\nabla} \left(\overrightarrow{\nabla} \cdot \overrightarrow{H} \right) - \overrightarrow{\nabla}^2 \overrightarrow{H}, \tag{A.2}$$

the second term on the right-hand side, $\overrightarrow{\nabla} \cdot \overrightarrow{H}$, vanishes as a consequence of Equation 2.2. Therefore,

$$\overrightarrow{\nabla} \times \left(\overrightarrow{\nabla} \times \overrightarrow{H} \right) = -\overrightarrow{\nabla}^2 \overrightarrow{H}, \tag{A.3}$$

$$= \overrightarrow{\nabla} \times \left(\overrightarrow{J} + \frac{\partial \overrightarrow{D}}{\partial t} \right), \tag{A.4}$$

$$= \overrightarrow{\nabla} \times \left(\sigma \overrightarrow{E} + \frac{\partial \left(\varepsilon \overrightarrow{E} \right)}{\partial t} \right), \tag{A.5}$$

$$= \sigma \overrightarrow{\nabla} \times \overrightarrow{E} + \varepsilon \frac{\partial \left(\overrightarrow{\nabla} \times \overrightarrow{E} \right)}{\partial t} \tag{A.6}$$

Additionally, Equation 2.3 allows writing:

$$\sigma \overrightarrow{\nabla} \times \overrightarrow{E} = -\mu\sigma \frac{\partial \overrightarrow{H}}{\partial t}, \tag{A.7}$$

$$\varepsilon \frac{\partial \left(\overrightarrow{\nabla} \times \overrightarrow{E} \right)}{\partial t} = -\mu\varepsilon \frac{\partial^2 \overrightarrow{H}}{\partial t^2}, \tag{A.8}$$

Combining with the constitutive relation Equation 2.6 yields the wave equation for the magnetic field:

$$\overrightarrow{\nabla}^2 \overrightarrow{H} - \mu\varepsilon \frac{\partial^2 \overrightarrow{H}}{\partial t^2} = \mu\sigma \frac{\partial \overrightarrow{H}}{\partial t}. \tag{A.9}$$

A.2 Polarization ellipse

The general expressions for the components of the electric field are :

$$\begin{cases} \overrightarrow{E}_x(z,t) = E_{0x}\cos(kz-\omega t)\,\hat{x}, \\ \overrightarrow{E}_y(z,t) = E_{0y}\cos(kz-\omega t+\delta)\,\hat{y}, \end{cases} \tag{A.10}$$

with $\delta = \varphi_y - \varphi_x$. Simultaneous algebraic and trigonometric manipulations of these expressions can be used to write

$$\frac{E_y(z,t)}{E_{0y}} - \frac{E_x(z,t)}{E_{0x}}\cos\delta = -\sin(kz-\omega t)\sin\delta. \tag{A.11}$$

Squaring Equation A.11 yields

$$\frac{E_x(z,t)^2}{E_{0x}^2} - -\frac{2E_x(z,t)E_y(z,t)}{E_{0x}E_{0y}}\cos\delta + \frac{E_y(z,t)^2}{E_{0y}^2}\cos^2\delta = \sin^2(kz-\omega t)\sin^2\delta, \tag{A.12}$$

$$= \left(1-\cos^2(kz-\omega t)\right)\sin^2\delta, \tag{A.13}$$

$$= \left(1-\frac{E_x(z,t)^2}{E_{0x}^2}\right)\sin^2\delta. \tag{A.14}$$

Eventually, the expression of the ellipse is obtained by rewritng the last expression:

$$\frac{E_x(z,t)^2}{{E_{0x}}^2} - \frac{2E_x(z,t)E_y(z,t)}{E_{0x}E_{0y}}\cos\delta + \frac{E_y(z,t)^2}{{E_{0y}}^2} = \sin^2\delta. \tag{A.15}$$

Appendix B

Supplementary figures

B.1 Jones pupil matrices

B.1.1 Beacon wavelength

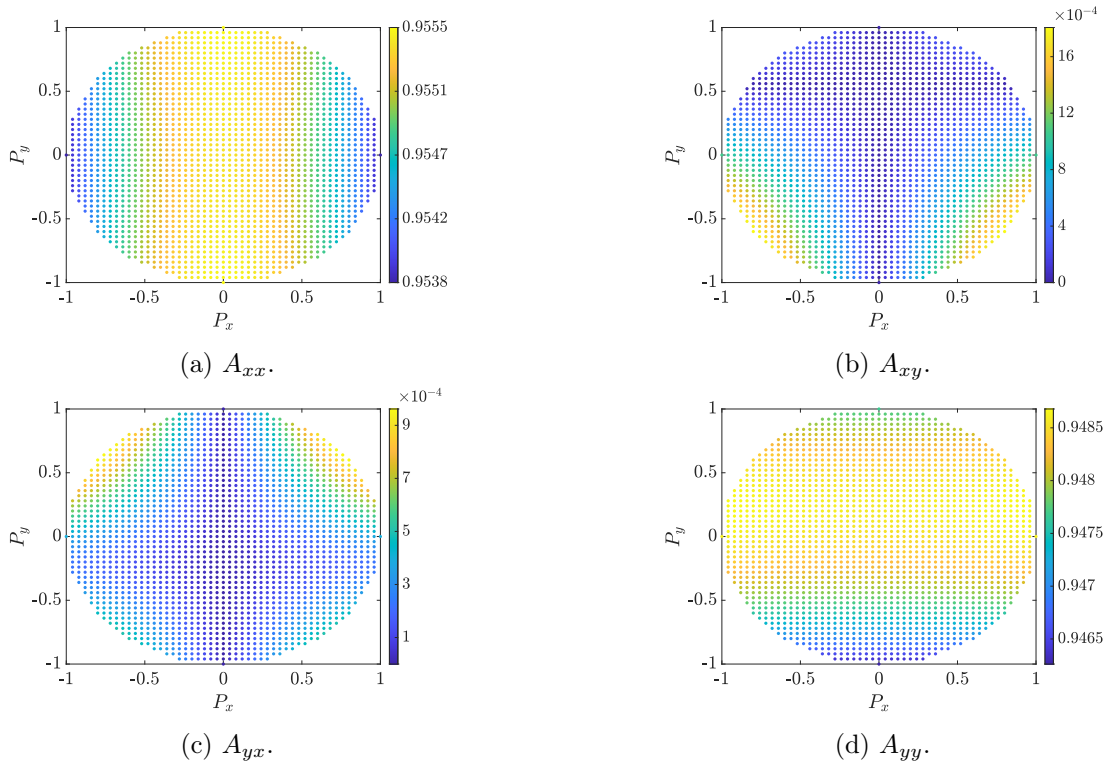

(a) A_{xx}. (b) A_{xy}.

(c) A_{yx}. (d) A_{yy}.

Figure B.1 – **Amplitude coefficients of the Jones pupil matrices for $\lambda = 685$ nm.**

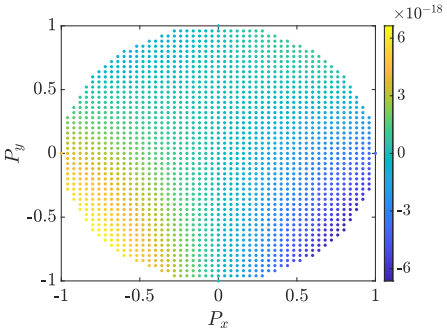

(a) φ_{xx} [°].

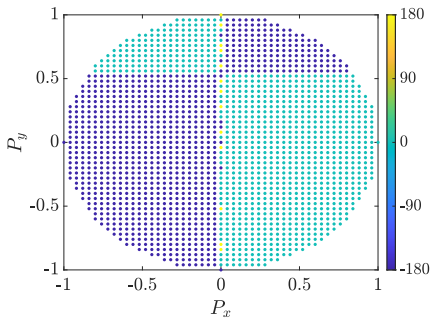

(b) φ_{xy} [°].

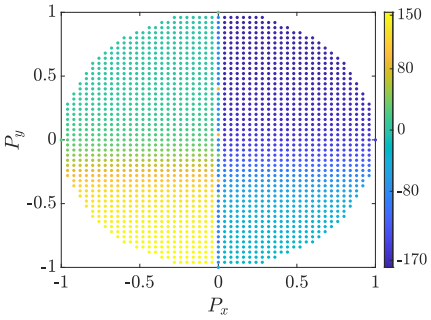

(c) φ_{yx} [°].

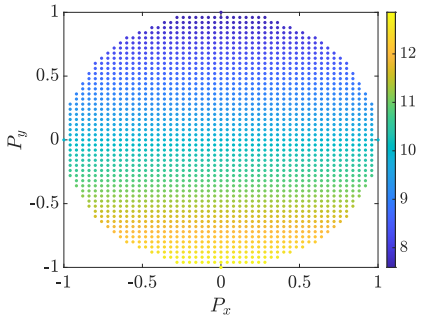

(d) φ_{yy} [°].

Figure B.2 – **Phase coefficients of the Jones pupil matrices for $\lambda = 685$ nm.**

B.1.2 Telecommunication wavelength

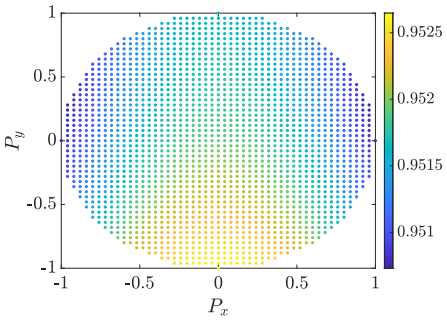

(a) A_{xx}.

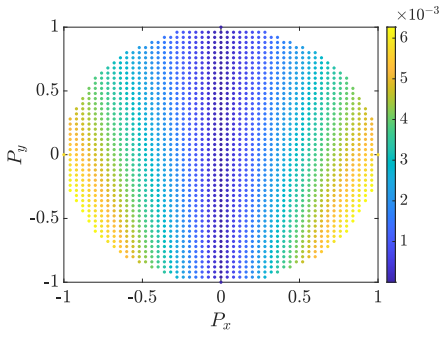

(b) A_{xy}.

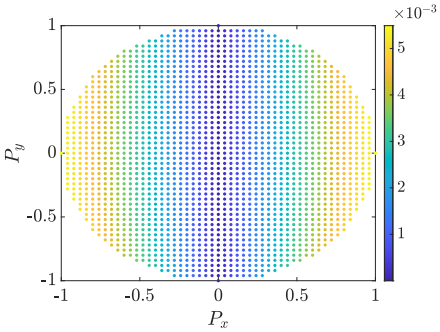

(c) A_{yx}.

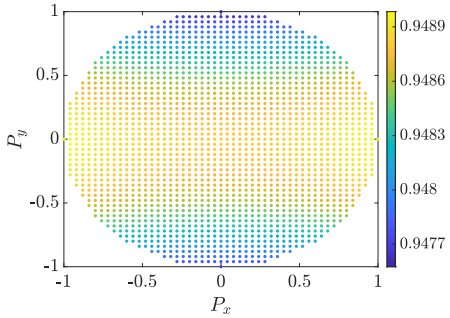

(d) A_{yy}.

Figure B.3 – **Amplitude coefficients of the Jones pupil matrices for $\lambda = 1550$ nm.**

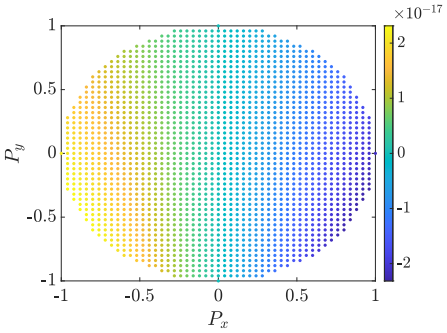

(a) φ_{xx} [°].

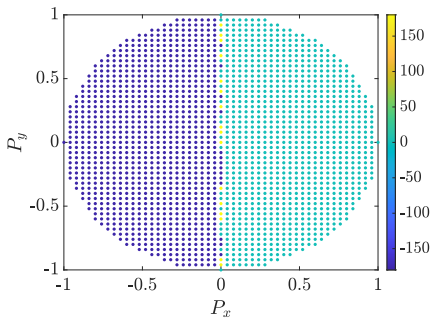

(b) φ_{xy} [°].

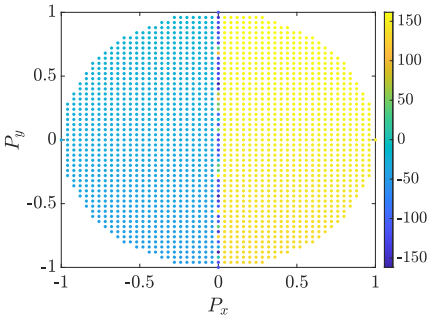

(c) φ_{yx} [°].

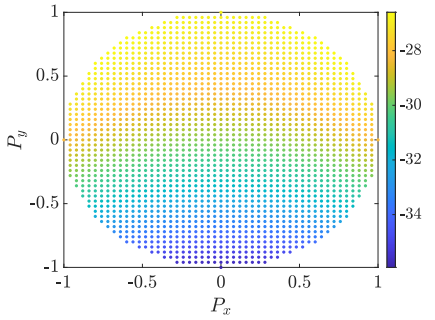

(d) φ_{yy} [°].

Figure B.4 – **Phase coefficients of the Jones pupil matrices for $\lambda = 1550$ nm.**

Bibliography

Advanced Mechanical and Optical Systems (AMOS) (2024) About us.

Anche RM, Ashcraft JN, Haffert SY, Millar-Blanchaer MA, Douglas ES, Snik F, Williams G, van Holstein RG, Doelman D, Gorkom KV, Skidmore W (2023) Polarization aberrations in next-generation giant segmented mirror telescopes (gsmts). *Astronomy & Astrophysics* .

Arteaga-Díaz P, Parra-Serrano M, Denisenko N, Fernandez V (2020) Correcting polarization degradation in free-space qkd systems In *2020 22nd International Conference on Transparent Optical Networks (ICTON)*, pp. 1–4.

Aspnes DE (1974) Optimizing precision of rotating-analyzer ellipsometers. *J. Opt. Soc. Am.* 64:639–646.

Azzam R, Bashara N (1987) *Ellipsometry and Polarized Light*, Vol. 2 North-Holland Publishing Company.

Born M, Wolf E (1999) *Principles of Optics* Cambridge University Press, 7 edition.

Chaabani S (2023) Master thesis and internship - master's thesis: Advances in free-space quantum key distribution - integration internship: Centre spatial de liège Master's thesis, Université de Liège, Liège, Belgique Unpublished master's thesis.

Chipman RA (1987) Polarization aberrations. *Journal of the Optical Society of America* .

Chipman RA, Lama WST, Breckinridgea J (2015) Polarization aberration in astronomical telescopes. *Astronomical Society of the Pacific* .

Clarke D (2010) *Stellar Polarimetry* WILEY-VCH Verlag GmbH & Co. KGaA.

Collett E (2005) *Field Guide to Polarization*, Vol. 6 SPIE Press.

Crabtree K (2007) Polarization critical optical systems: Important effects and design techniques Technical report Opti 521, College of Optical Sciences, The University of Arizona.

Dawar A (2007) *Quantum Computing* University of Cambridge.

Edmund Optics (2024) Understanding waveplates and retarders Edmund Optics.

Fabricius H, Hansen TN (2008) Optimizing the phase retardation caused by optical coatings In Kaiser N, Lequime M, Macleod HA, editors, *Advances in Optical Thin Films III*, Vol. 7101, p. 71011I. International Society for Optics and Photonics, SPIE.

Glendinning I (2005) *The Bloch Sphere* Portland State University.

Gonçalves D, Irene E (2002) Fundamentals and applications of spectroscopic ellipsometry. *Química Nova* 25.

Hayt WH, Buck JA (2001) *Engineering Electromagnetics*, Vol. 6 McGraw-Hill.

He W, Fu Y, Liu Z, Zhang L, Wang J, Zheng Y, Li Y (2017) Three-dimensional polarization aberration functions in optical system based on three-dimensional polarization ray-tracing calculus. *SPIE* .

Jones RC (1941) A new calculus for the treatmant of optical systems, i. description and discussion of the calculus. *Journal of the Optical Society of America* .

Klein M, Furtak T (1986) *Optics* Wiley series in pure and applied optics. Wiley.

Miller S, Jiang L, Pau S (2022) Birefringent coating to remove polarization aberrations. *Opt. Express* 30:20629–20646.

Motschmann H, Teppner R (2001) Ellipsometry in interface science. *Studies in Interface Science* 11:1–42.

Neutelings I (2018) Physik ii Physik-Institut Universität Zürich.

Riebesell J, Bringuier S (2020) Collection of standalone tikz images Cambridge University.

Scharf T (2007) *Polarized light in liquid crystals and polymers* John Wiley & Sons, Inc.

SENTECH Instruments (2024) Senresearch 4.0 spectroscopic ellipsometer Technical report, SENTECH Instruments, Schwarzschildstraße 2, 12489 Berlin, Germany.

Tompkins H, Irene E (2005) *Handbook of Ellipsometry* Elsevier Science.

Tsagkaropoulos A (2021) Polarization University of Athens.

Vanderheyden B (2023) *Electromagnetisme* Univerisité de Liège.

Wang JY, Yang B, Liao SK, Zhang L, Shen Q, Hu XF, Wu JC, Yang SJ, Jiang H, Tang YL, Zhong B, Liang H, Liu WY, Hu YH, Huang YM, Qi B, Ren JG, Pan GS, Yin J, Jia JJ, Chen YA, Chen K, Peng CZ, Pan JW (2013) Direct and full-scale experimental verifications towards ground–satellite quantum key distribution. *Nature Photonics* 7:387–393.

Wolf R (2021) *Quantum Key Distribution*, Vol. 988 Springer.

Wolski A (2011) *Theory of electromagnetic fields* University of Liverpool, and the Cockcroft Institute.

Wu J, Zhang L, Jia J, Wang T, Shu R, He Z, Wang J (2020) Polarization-maintaining design for satellite-based quantum communication terminals. *Opt. Express* 28:10746–10759.

Zhang Q, Song H, Lucas K (2007) Polarization aberration modeling via Jones matrix in the context of OPC In Naber RJ, Kawahira H, editors, *Photomask Technology 2007*, Vol. 6730, p. 67301Q. International Society for Optics and Photonics, SPIE.

Zhang Y, Bian Y, Li Z, Yu S, Guo H (2024) Continuous-variable quantum key distribution system: Past, present, and future. *Applied Physics Reviews* 11:011318.